geosciences

MDPI

Article

Record of Crustal Thickening and Synconvergent Extension from the Dajiamang Tso Rift, Southern Tibet

William B. Burke [1,*], Andrew K. Laskowski [1], Devon A. Orme [1], Kurt E. Sundell [2], Michael H. Taylor [3], Xudong Guo [4] and Lin Ding [4]

[1] Department of Earth Sciences, Montana State University, Bozeman, MT 59715, USA; andrew.laskowski@montana.edu (A.K.L.); devon.orme@montana.edu (D.A.O.)
[2] Department of Geosciences, University of Arizona, Tuscon, AZ 85721, USA; sundell@arizona.edu
[3] Department of Geology, University of Kansas, Lawrence, KS 66045, USA; mht@ku.edu
[4] Institute of Tibetan Plateau Research, Chinese Academy of Sciences, Beijing 100049, China; guoxudong@itpcas.ac.cn (X.G.); dinglin@itpcas.ac.cn (L.D.)
* Correspondence: williambrianburke@gmail.com

Abstract: North-trending rifts throughout south-central Tibet provide an opportunity to study the dynamics of synconvergent extension in contractional orogenic belts. In this study, we present new data from the Dajiamang Tso rift, including quantitative crustal thickness estimates calculated from trace/rare earth element zircon data, U-Pb geochronology, and zircon-He thermochronology. These data constrain the timing and rates of exhumation in the Dajiamang Tso rift and provide a basis for evaluating dynamic models of synconvergent extension. Our results also provide a semi-continuous record of Mid-Cretaceous to Miocene evolution of the Himalayan-Tibetan orogenic belt along the India-Asia suture zone. We report igneous zircon U-Pb ages of ~103 Ma and 70–42 Ma for samples collected from the Xigaze forearc basin and Gangdese Batholith/Linzizong Formation, respectively. Zircon-He cooling ages of forearc rocks in the hanging wall of the Great Counter thrust are ~28 Ma, while Gangdese arc samples in the footwalls of the Dajiamang Tso rift are 16–8 Ma. These data reveal the approximate timing of the switch from contraction to extension along the India-Asia suture zone (minimum 16 Ma). Crustal-thickness trends from zircon geochemistry reveal possible crustal thinning (to ~40 km) immediately prior to India-Eurasia collision onset (58 Ma). Following initial collision, crustal thickness increases to 50 km by 40 Ma with continued thickening until the early Miocene supported by regional data from the Tibetan Magmatism Database. Current crustal thickness estimates based on geophysical observations show no evidence for crustal thinning following the onset of E–W extension (~16 Ma), suggesting that modern crustal thickness is likely facilitated by an underthrusting Indian lithosphere balanced by upper plate extension.

Keywords: Tibet; E–W extension; crustal thickness; T/REE geochemistry; geochronology; thermochronology

Citation: Burke, W.B.; Laskowski, A.K.; Orme, D.A.; Sundell, K.E.; Taylor, M.H.; Guo, X.; Ding, L. Record of Crustal Thickening and Synconvergent Extension from the Dajiamang Tso Rift, Southern Tibet. *Geosciences* **2021**, *11*, 209. https://doi.org/10.3390/geosciences11050209

Academic Editors: Rodolfo Carosi, Mario da Costa Campos Neto, Haakon Fossen, Chiara Montomoli, Matteo Simonetti and Jesus Martinez-Frias

Received: 25 March 2021
Accepted: 10 May 2021
Published: 12 May 2021

1. Introduction

Normal fault systems accommodating orogen-parallel extension provide an opportunity to study the dynamics of synconvergent extension in contractional orogenic belts [1]. In the Lhasa terrane of southern Tibet, we calculate quantitative crustal thickness estimates calculated from trace/rare earth element geochemistry, U-Pb geochronology, and zircon-He (ZHe) thermochronology to examine the relationship between crustal thickness trends and the timing/dynamics of E–W extension in one of the worlds archetypal collisional orogens. Assembled by the sequential accretion of island arc terranes and continental fragments since the Paleozoic, the Tibetan Plateau is the highest and most expansive orogenic plateau on Earth with crustal thickness estimates ranging from ~65 km in the north [2,3] to ~85 km beneath the Indus-Yarlung suture [4]. While contractional deformation has led to significant shortening and crustal thickening throughout the region [5–8], the southern and

central portions of the Tibetan Plateau have experienced east–west extension since the early Neogene, expressed at the surface as a network of approximately north-striking normal faults and associated strike slip faults [1,9,10]. A fundamental question in understanding this orogen is how crustal thickness has changed through time and how these changes relate to ongoing east–west extension [11].

Traditionally, estimates of crustal thickness beneath Tibet have relied largely on geophysical observations, with important findings contributed by the INDEPTH (International Deep Profiling of Tibet and the Himalaya) [2,12–17] and Hi-CLIMB (Himalayan-Tibetan Continental Lithosphere during Mountain Building) [18] projects. While these geophysical initiatives have proven extremely valuable for evaluating modern sub-surface structures, they are less useful when estimating crustal thickness in the geologic past. To quantitatively estimate crustal thickness, recent studies have calibrated trace/rare earth element (T/REE) ratios of intermediate igneous rocks in arc settings where Moho depth is well constrained by seismic observations [19–21]. Further refinement of partition coefficients for T/REEs have allowed for more robust estimation of whole rock chemistry from individual zircon minerals [22], making these calculations applicable to single grain analytical techniques (e.g., LA-ICP-MS). When coupled with geochronologic analysis from the same sample, these proxies provide time-sensitive, quantitative crustal thickness estimates that can be used as a test of competing models for the development of ancient orogenic systems.

To understand how ongoing east–west extension relates to these crustal thickness trends, we focus our attention on north-striking normal faults concentrated in the central and southern portions of the Lhasa terrane of southern Tibet. These normal faults can be divided into two classes, herein referred to as Tibetan and Gangdese rifts (Figure 1). We define Tibetan rifts as terrane-scale rift valleys (>150 km in length) that generally strike between 0° and 30°. We define Gangdese rifts as small-scale (<150 km in length) rifts localized to high topography in the Gangdese Range located along the southern margin of the Lhasa terrane, generally striking between 330° and 0°. Numerous studies have focused on constraining the plateau's recent phase of east–west extension along Tibetan rifts [23–27]; however, the difference in dynamics between these regional-scale features and Gangdese rifts has only been investigated by few [6].

Previous studies on east–west extension have led to several leading dynamic models for syncontractional extension along the Himalayan-Tibetan orogen. These include:

1. Lateral collapse of the plateau as a result of gravitational potential energy outweighing collisional forces [28–30].
2. Convective removal of the lower layer of Tibet's over-thickened lithosphere [31].
3. Coeval thickening and collapse driven by an underthrusting Indian lithosphere [2,25,32].
4. Progressive development of east–west extension controlled by arc curvature [33].
5. Extension initiation timing controlled by lateral migration of slab detachment [34].

Each of these models calls for a different driving mechanism to explain the onset of east–west extension in the Lhasa terrane in southern Tibet. To test these competing models, we present new geologic mapping, U-Pb geochronology, ZHe thermochronology, Lu-Hf isotope geochemistry, and T/REE crustal thickness estimates from a Gangdese rift just north of the Indus-Yarlung suture, herein referred to as the Dajiamang Tso rift (Figure 1). These data provide further insight into the timing of east–west exhumation events throughout the plateau, as well as time-sensitive crustal thickness estimates spanning the proposed period of India-Eurasia collision.

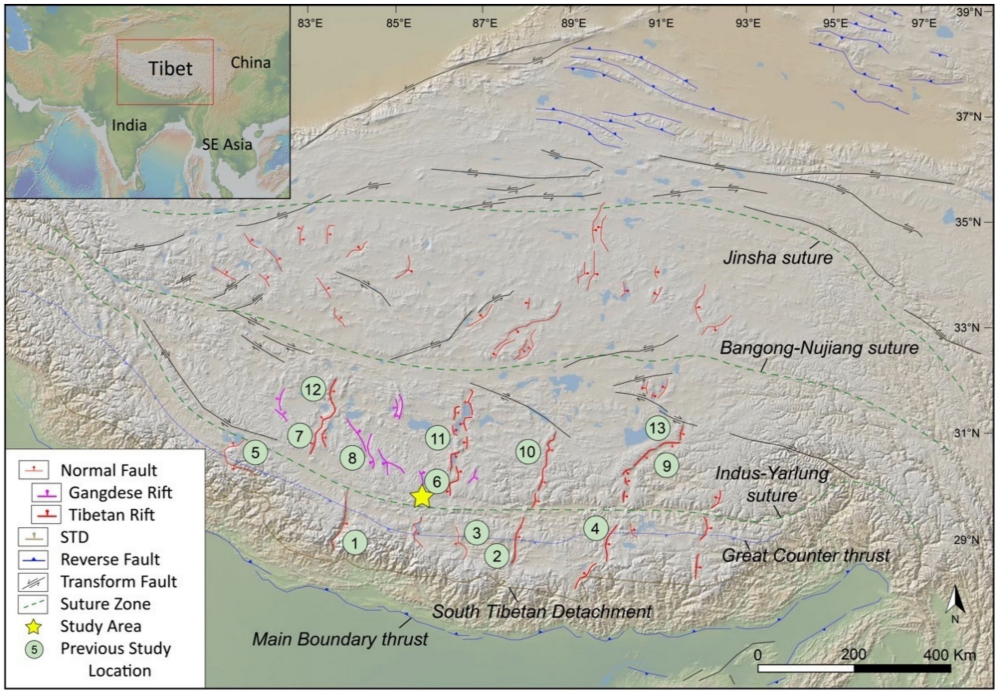

Figure 1. Topographic map of the Tibetan Plateau highlighting major deformational structures and suture zones adapted from Taylor and Yin (2009) [35]. The basemap is a global multi-resolution topography (GRMT) synthesis digital elevation model rendered in the GeoMapApp (geomapapp.org). Numbered green dots represent locations of previous studies investigating Miocene extension in central and southern Tibet, adapted from Sundell et al. (2013) [23]. Studies are labeled with numbers increasing from SSW to NNE (measured orthogonal to the Indus-Yarlung suture zone): 1. Thakkhola graben [36], 2. Arma Drime massif [37], 3. Kung Co graben [38], 4. Ringbung graben [39], 5. Gurla Mandhata dome [40,41], 6. Daggyai Tso graben [42,43], 7. South Lunggar rift [24], 8. Lopu Kangri rift [43–45], 9. Nyainquentanghala Shan [46,47], 10. Pum Qu-Xanza rift [48], 11. Tangra Yumco graben [27,49], 12. North Lunggar rift [23,50], 13. Gulu rift [51].

2. Geologic Setting

2.1. Rock Units

The Dajiamang Tso rift is located in the Gangdese Range (a.k.a. the Transhimalaya Range) of southern Tibet. This region is located within the Lhasa terrane immediately north of the Indus-Yarlung suture and comprises four major lithologic units. The northernmost of these is the Linzizong Formation [52], a nonmarine sedimentary unit containing volcanic and volcaniclastic rocks of Late Cretaceous-Early Paleogene age [53–56]. Linzizong volcanic rocks are interpreted to be genetically liked with plutonic igneous rocks of the Gangdese Batholith, which mainly crop out to the south in the Dajiamang Tso region (Figure 2). These calc-alkaline intrusive rocks of the Gangdese Batholith [57–59] comprise the second major unit in the southern Gangdese Range and are roughly age-equivalent to the overlying Linzizong volcanic rocks. Formation histories of both lithologic units are associated with continental arc magmatism as a result of northward subduction of the Neo-Tethyan lithosphere during the Late Cretaceous-Paleogene [52].

Nonmarine, conglomeratic strata equivalent to the Kailas Formation [60–62] are well exposed to the south of the Gangdese Batholith rocks (Figure 2). Detrital and igneous zircon U-Pb ages constrain the timing of deposition to the Oligocene-Miocene transition [60], with work by Leary et al. (2016) [61] identifying a trend of younging deposition from 26–24 Ma in western Tibet (81° E) to 23–22 Ma in the east near Dazhuka (89.8° E). Farthest South, the Cretaceous-Paleogene Xigaze forearc strata [63–70] are juxtaposed against Kailas Formation strata across a steeply south-dipping reverse fault (Figure 2).

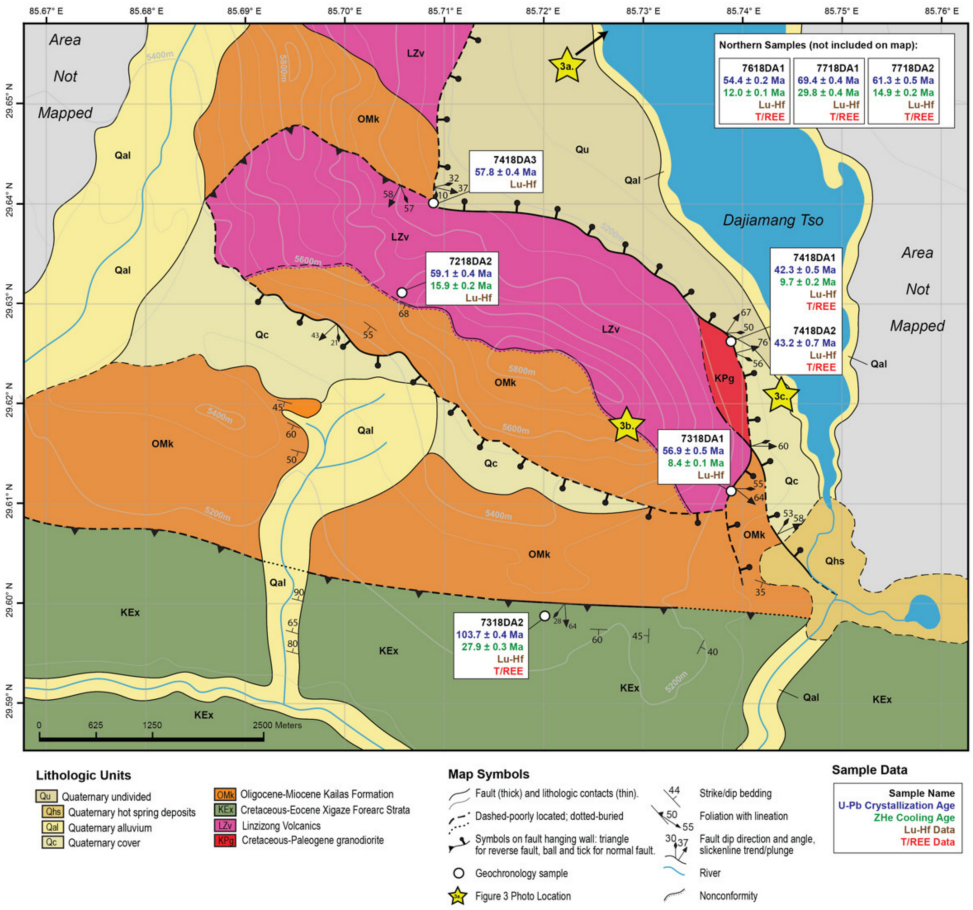

Figure 2. Geologic map of the Dajiamang Tso rift field area (1:40,000 scale) highlighting lithologic units, structures, and sample locations. Sample locations are represented by white circles, with the sample name, U-Pb geochronology crystallization age, ZHe thermochronology cooling age, and indicators for Hf and T/REE datasets included in adjacent information panels. Gold stars represent the locations of the field photos. Data for overlapping structural measurements were averaged for map clarity. Information panels for three samples collected north of the mapping area are also provided in the top right corner of the map.

2.2. *Fault Systems*

2.2.1. The Great Counter Thrust

The most pronounced contractional structure in the southern Gangdese Range is a system of south-dipping reverse faults referred to as the Great Counter thrust, which places Xigaze forearc strata in the hanging wall on top of Kailas Formation strata in the footwall in the region north of the Indus-Yarlung suture zone [71–73]. Initiation of the Great Counter thrust system is interpreted at ca. 23 Ma based on provenance changes and clast compositions in the upper Kailas Formation in the Lazi region of southern Tibet [60], with the younger limit for activity constrained by the transition from north–south contraction to east–west extension in the region, evidenced by Tibetan rifts cross-cutting the Great Counter thrust in several locations [26]. Earliest estimates for the onset of east–west extension range from ca. 18 Ma to 14 Ma [24,41,43–45], requiring that the Great Counter thrust was inactive by this time. Despite its exposure throughout much of southern Tibet, slip magnitudes along this thrust system remain poorly constrained due to erosion or burial of the hanging wall and footwall cutoffs, respectively.

2.2.2. Gangdese Rifts

The southern and central Tibetan Plateau is in a current constrictional strain state dominated by orogen parallel extension, as indicated by the current GPS velocity field [74]. North-striking Tibetan rifts crosscut the entire Lhasa terrane, are kinematically connected

with strike-slip structures along the Bangong-Nuinag suture zone and the Qiangtang terrane, and are consistent with and accommodate the current GPS velocity field (Figure 1) [10,23]. Along the southern boundary of the Lhasa terrane, Gangdese rifts constitute a subset of Tibetan rifts, characterized by shorter along-strike lengths (<150 km). These extensional structures are localized in the high topography area of the Gangdese drainage divide (Figure 1) [6]. Gangdese rifts are commonly expressed as a central horst block bounded by moderate-to-steeply east and west-dipping normal faults. The horst blocks are high relief ranges with range-bounding normal faults cutting quaternary sediments along their base, and locally, active hot spring and associated tuff deposits observed at lower elevations (Figure 2).

3. Methods

3.1. Field Methods and Sample Preperation

Geological mapping was conducted for a ~100 km^2 field area along the southern portion of the Dajiamang Tso rift (Figure 2). Field data stations (n = 33) were plotted using 1:40,000 scale topographic base maps augmented with Landsat imagery to make structural observations of fault-related features and observe structural relationships of lithologic units. Nine samples were collected for geochronological, thermochronological, and geochemical analysis. Samples were separated at the Institute of Tibetan Plateau Research in Beijing, China using standard disaggregation, density, and magnetic separation techniques.

3.2. Zircon U-Pb Geochronology

Igneous zircon grains (n = 20 to n = 50) for each sample were mounted on 1-inch diameter epoxy pucks alongside crystal standards FC [75,76], R33 [77], and SL [78]. Mounts were polished to ~20 um to reveal crystal cores and subsequently imaged using backscatter electron and cathodoluminescence techniques for navigation purposes and further grain evaluation. U-Pb geochronology was conducted at the Arizona LaserChron Center (ALC) using Laser Ablation-Inductively Coupled Plasma-Mass Spectrometry (LA-ICP-MS) following techniques in Gehrels et al. (2006, 2008) [78,79] and Gehrels and Pecha (2014) [80]. Analyses used a Photon Machines G2 laser connected to an Element 2 ICP-MS with a jet pump and interface [81]. Spot sizes measured 20 um and ablation pits were ~15 um deep, with analyses conducted with an Element 2 ICP-MS. Reported weighted mean ages were calculated using the TuffZirc algorithm [82] from Berkley Geochronology Center's ISOPLOT program [83]. This program is designed to produce reliable ages from complex zircon aliquots, while eliminating the bias that comes with manually trimming datasets to obtain clusters with MSWDs close to 1. The program ranks grains by $^{206}Pb/^{238}U$ age, then calculates the median age of the largest cluster that yields a "probability of fit" >0.05 [82]. For unknowns, grains with $^{206}Pb/^{238}U$ and $^{206}Pb/^{207}Pb$ errors greater than 10% were rejected, as well as grains with discordance greater than 20%. Inherited grains were analyzed, but not included in some final weighted mean plots to ensure a visible scale. Reported ages do not reflect external (systematic) uncertainties. Full analytical details can be viewed in Supplementary Table S1.

3.3. Lu-Hf Isotope Geochemistry

Single-grain Lu-Hf isotope geochemistry using LA-ICP-MS was conducted at ALC for a subset of zircon (n = 4 to n = 11) from all nine samples. Ablation used a Photon Machines Analyte G2 excimer laser equipped with a HelEx cell and the analysis used a Nu Plasma HR ICP-MS. Grains whose U-Pb analysis were used to calculate the weighted mean age for each sample were targeted for Lu-Hf analysis, while grains with discordant or imprecise ages were not analyzed. Hf analyses used a spot size of 40 um and were conducted on top of U-Pb analysis pits to ensure that Hf isotopic data were determined from the same crystal domain as the U-Pb age [80].

3.4. Zircon Trace/Rare Earth Element Geochemistry

Single-grain trace/rare earth element geochemical analyses of zircon was conducted at ALC using LA-ICP-MS. T/REE analyses were conducted on the same Element 2 ICP-MS as U-Pb geochronology. Analyses of each grain involved measurement of 23 trace and rare earth elements, as well as elements used for U-Th-Pb geochronology, including ^{27}Al, ^{29}Si, ^{31}P, ^{45}Sc, ^{49}Ti, ^{89}Y, ^{93}Nb, ^{139}La, ^{140}Ce, ^{141}Pr, ^{146}Nd, ^{152}Sm, ^{153}Eu, ^{157}Gd, ^{159}Tb, ^{164}Dy, ^{165}Ho, ^{166}Er, ^{169}Tm, ^{174}Yb, ^{175}Lu, ^{177}Hf, ^{161}Ta, ^{202}Hg, ^{204}(Hg + Pb), ^{206}Pb, ^{207}Pb, ^{208}Pb, ^{232}Th, ^{235}U, and ^{238}U, with dwell times ranging from 0.001 to 0.3 s. T/REE analyses used a spot size of 30 um and were conducted on top of U-Pb analysis pits following procedures outlined in Gehrles and Pecha (2014) for Lu-Hf analyses [80]. Whole rock geochemistry was subsequently calculated following procedures discussed in Chapman [22], previously applied to detrital zircon grains.

3.5. Zircon-He Thermochronology

ZHe thermochronology was performed on the same suite of samples at the Arizona Radiogenic Helium Dating Laboratory at the University of Arizona following procedures outlined in Reiners (2005) [84]. Five grains from each sample were hand-selected based on size (diameter >60 um), morphology (subhedral to euhedral), lack of inclusions, and optical clarity. High resolution photomicrographs were used to measure and record crystal dimensions following procedures outlined in in Hourigan et al. (2005) [85], with euhedral grains with geometric morphologies favored to more accurately estimate alpha-ejection corrections. Measured grains were subsequently packaged in ~1 mm Nb foil envelopes to ensure even ablation during analyses. Zircons in Nb foil packets were loaded into a vacuum laser cell and individually heated for 15 min using a focused beam from a 1–2 W laser to extract 4 He gas. Zircon packets were then reheated at least one time for 15 min until 4 He yields were less than 2% of the compounded total. ^{4}He/^{3}He ratios were measured using a quadrupole mass spectrometer equipped with a Channeltron electron multiplier. Fish Canyon Tuff (FCT) standards with a (U-Th)/He age of 28.48 $\pm$ 0.06 Ma (2σ) [76] were analyzed between every group of five unknowns [84]. Grains that yielded high effective uranium (eU = U + 0.235 $\times$ Th), a proxy for radiation damage [86], were further examined within their structural context when interpreting sample cooling ages.

3.6. HeFTy Thermal Modeling

Inverse modeling was conducted using the software program HeFTy version 1.9.3 [87] to test a range of thermal histories that could provide good fits to data generated by ZHe thermochronology. This approach utilizes a Monte Carlo algorithm that generates thermal histories (n = 10,000) based on search constraints in the model's time–temperature space. Characteristics (raw date, ppm U, ppm Th) from euhedral zircon grains with minimal inclusions and radii >35 um were used for model runs. HeFTy inverse modeling was executed based on calibrations from Guenthner et al. (2013) [86] and He diffusion characteristics (stopping distances) from Ketcham et al. (2011) [88]. The searchable space for time–temperature paths was defined by the following input parameters:

1. Zircons extracted from extrusive samples were erupted at surface temperatures between 0 and 20 °C at the time of crystallization measured by U-Pb geochronology.
2. Zircons extracted from intrusive samples were exposed to temperatures between 700 °C and 900 °C at the time of crystallization measured by U-Pb geochronology.
3. ZHe cooling ages require burial of extrusive samples to at least 140–200 °C (within the ZHe partial retention zone) [86] following crystallization.
4. Samples were collected at surface temperatures between 0 °C and 20 °C at 0 Ma.

3.7. Crustal Thickness Calculations

Ratios of pressure-sensitive trace/rare earth elements such as Sr/Y and La/Yb have been calibrated to provide quantitative estimates of crustal thickness in orogenic settings where Moho depth is well constrained by seismic observations [19–21]. These ratios rely

on the preferential incorporation of Sr and La into minerals such as plagioclase at low pressures and temperatures, and Y and Yb into minerals including garnet and amphibole at higher pressure temperature conditions [19]. Thus, magmas that undergo partial melting at greater depths will have relatively high Sr/Y and La/Yb ratios compared to those generated in settings with lower crustal thicknesses.

Empirical calibration of these ratios to modern crustal thicknesses was conducted by Profeta et al. (2015) [19], allowing application to orogenic settings hosting igneous rocks of intermediate composition. Geochemical data were filtered to include rocks with 55–68 wt.% SiO_2, 0–4% MgO, and average Rb/Sr ratios between 0.05 and 0.2 to exclude ultramafic/mantle-derived melts, high silica granites, and rocks formed by partial melting of pre-existing metasedimentary rocks [21]. Recent work by Sundell et al. (2021) [89] revisited and recalibrated these ratios to better account for extreme crustal thickness estimated from high ratios and application to the Himalayan-Tibetan orogen. Assuming similar partition coefficients for zircon within the melt, single grain zircon T/REE abundances were converted to whole rock geochemistry and normalized to Chondrite-normalized Uniform Reservoir (CHUR) after Chapman et al. (2016) [22], allowing for application to the revised crustal thickness equation from Sundell et al. (2021) [89]:

$$dm = (17.0 \pm 3.7) \times \ln(La/Ybn) + (6.9 \pm 5.8) \text{ (at } 2\sigma), \quad (1)$$

where dm refers to the depth of the crust–mantle boundary (crustal thickness). Crustal thickness estimates are reported with a $\pm$ 10.8 km (2σ) uncertainty based on residuals from proxy recalibration [89].

3.8. Compilation of Geochemical Data for South-Central Tibet

To evaluate Lu-Hf isotope and single-grain zircon T/REE geochemical data produced from this study in a regional context, previously published whole-rock geochemical data from southern Tibet were downloaded from the Tibetan Magmatism Database on 23 March 2020 [90]. Each dataset was filtered to include samples collected between 28–32° North and 82–92° East, with U-Pb crystallization ages $\leq$200 Ma. For T/REE geochemistry, data were further filtered using the parameters of Profeta et al. (2015) [21], as mentioned in the previous section. From this reduced dataset, quantitative crustal thickness estimates were calculated using the approach of Sundell et al. (2021) [89].

4. Results

4.1. Geologic Mapping Results

4.1.1. Rock Units and Correlations

The northernmost rocks in the Dajiamang Tso rift field area are porphyritic rhyolite with quartz-feldspar phenocrysts and pyroclastic flow deposits with incorporated volcaniclastic sandstone clasts (Figure 2). We correlate these rocks with the Paleocene-Eocene volcanic and volcaniclastic rocks of the Linzizong Formation [52]. In the eastern third of the map area, quartz-feldspar-biotite granodiorite locally intruded by aphanitic dikes shares an intrusive contact with the rhyolite unit. We correlate these rocks to the Cretaceous-Paleogene calc-alkaline intrusive rocks of the Gangdese Batholith [57]. In the central portion of the map area, sandstone and cobble-boulder conglomerate containing porphyritic andesite is exposed. We correlate these rocks with Oligocene-Miocene nonmarine conglomeratic strata of the Kailas Formation based on similar facies and clast compositions exposed along the suture zone [58–62]. The southernmost rocks of the Dajiamang Tso rift field area are litharenites and re-worked tuff, which we correlate to forearc basin strata of the Cretaceous-Paleogene Xigaze Group, part of the forearc basin in southern Tibet [62–69].

4.1.2. Fault Systems

In the southern portion of the map area, Xigaze forearc strata are juxtaposed atop nonmarine strata of the Kailas Formation along a moderately south-dipping, top-to-the-

north reverse fault (Figure 2). This fault dips approximately 64° to the south and exhibits fault grooves consistent with a top-to-the-northeast oblique sense of motion. We interpret this structure to represent a splay of the regionally extensive Great Counter thrust system (Figure 1) [71–73]. Approximately 4 km north of the Great Counter thrust splay, Linzizong Formation volcanic and volcaniclastic rocks are juxtaposed against Kailas Formation strata in the hanging wall of a second steeply south-dipping, top-to-the-north reverse fault. Exposure of this structure is limited; however, similar geometries and kinematics lead us to interpret that this fault is likely a splay of the Great Counter thrust system.

The Dajiamang Tso rift is characterized by a central horst block bound by two moderate-to-steeply dipping (43–76°) normal faults. The horst is expressed as a high relief range that exposes Gangdese Batholith granodiorite, Linzizong Formation volcanic rocks, and Kailas Formation strata (Figure 3). The range trends NW–SE in the central part of the field area before transitioning to a nearly N–S trend farther north. Hanging wall rocks are dominantly quaternary cover and are faulted directly against bedrock units constituting the central range-forming horst of the Dajiamang Tso rift. Quaternary cover and hot spring deposits are also cut by the range-bounding normal fault splays in the southeast portion of the mapping area. Tectonic geomorphology of this region also includes 2–3 m fault scarps, prominent triangular facets, and exposed fault surfaces.

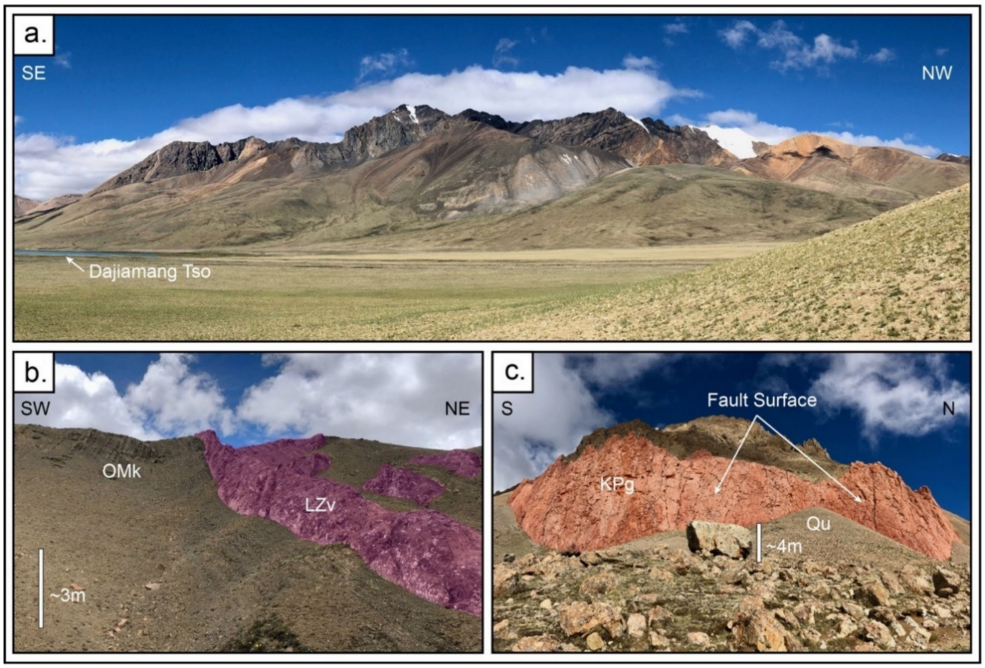

Figure 3. Selected field photos from the Dajiamang Tso rift mapping area: (**a**) Southwest-facing view of the Dajiamang Tso rift's central horst block, expressed as a roughly NNW–SSE trending high relief range; (**b**) Northwest-facing view of the depositional contact between Oligocene-Miocene nonmarine conglomeratic strata of the Kailas Formation (OMk) and Paleocene-Eocene volcanic rocks of the Linzizong Formation (LZv) (colored purple); (**c**) West-facing view of Cretaceous-Paleogene rocks of the Gangdese Batholith (KPg) (colored orange), displaying a major normal fault surface at the southeast extent of the range.

4.2. U-Pb Geochronology, Lu-Hf Geochemistry, and T/REE Geochemistry Results

Nine igneous samples were collected from bedrock exposures in the Dajiamang Tso rift region for zircon U-Pb geochronology, Lu-Hf isotope geochemistry, and T/REE geochemistry. Seven samples were collected from igneous outcrops located in the central horst structure of the rift, one sample was collected from a re-worked tuff in the hanging wall of the Great Counter thrust, and one sample was collected from a volcanic outcrop in the Dajiamang Tso rift valley. Igneous samples were divided into three groups based on their age distributions and rock type:

1. Volcanic and volcaniclastic rocks of the Linzizong Formation.
2. Gangdese batholith granodiorites and associated dikes and fault rocks.
3. Xigaze Group forearc rocks.

Many samples yielded MSWD's greater than 1, suggesting possible analysis of overlapping growth zones or incorporation of xenocrysts. Analytical results for each method can also be found in Supplementary Tables S1–S3. Full concordia plots can be found in Supplemental Figure S1.

4.2.1. Group 1: Linzizong Formation Volcanic Rocks

Sample 7318DA1 is porphyritic diorite with quartz and feldspar phenocrysts. This sample was collected just north of the Kailas basal contact in the footwall of the Dajiamang Tso rift in the southeast corner of the mapping area (Figure 2). Zircon U-Pb Geochronology for this sample produced a weighted mean age of 56.9 ± 0.5 Ma (n = 17, mean square weighted deviate (MSWD) = 1.7) (Figure 4). A total of 30 grains were analyzed, 0 were discordant, 2 grains were determined to be inherited (598.3 ± 4.9 and 211.5 ± 2.6 Ma) (not shown in Figure 4), and 17 were selected to calculate a mean sample age. Lu-Hf isotopic analysis for this sample yielded epsilon Hf values from −4.4 ± 0.9 to 0.4 ± 0.9 (Figure 5). No T/REE geochemical data were collected for this sample.

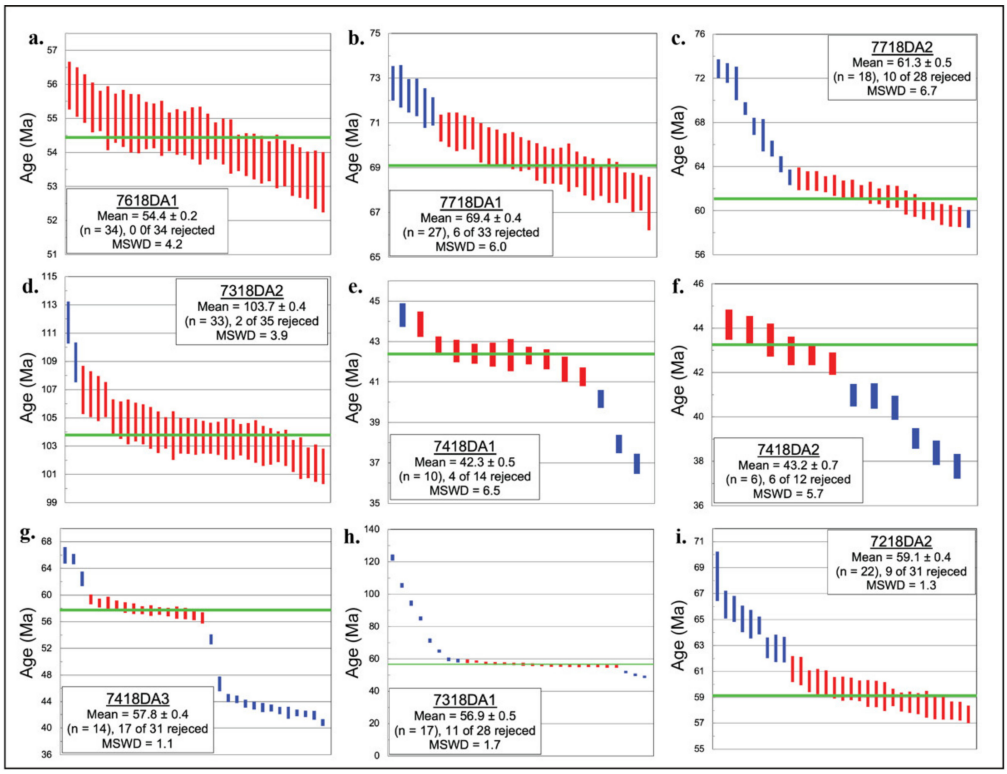

Figure 4. Zircon U-Pb geochronology weighted-mean age results by sample (**a–i**). Ages were calculated using the TuffZirc algorithm [82] from the Berkley Geochronology Center's ISOPLOT program [83]. Box heights are 2σ. Panels in the lower left of each graph display sample name, weighted-average crystallization age, sample size, and MSWD (mean square weighted deviate). Complete zircon U-Pb Geochronology results for individual grains can be found in Supplementary Table S1.

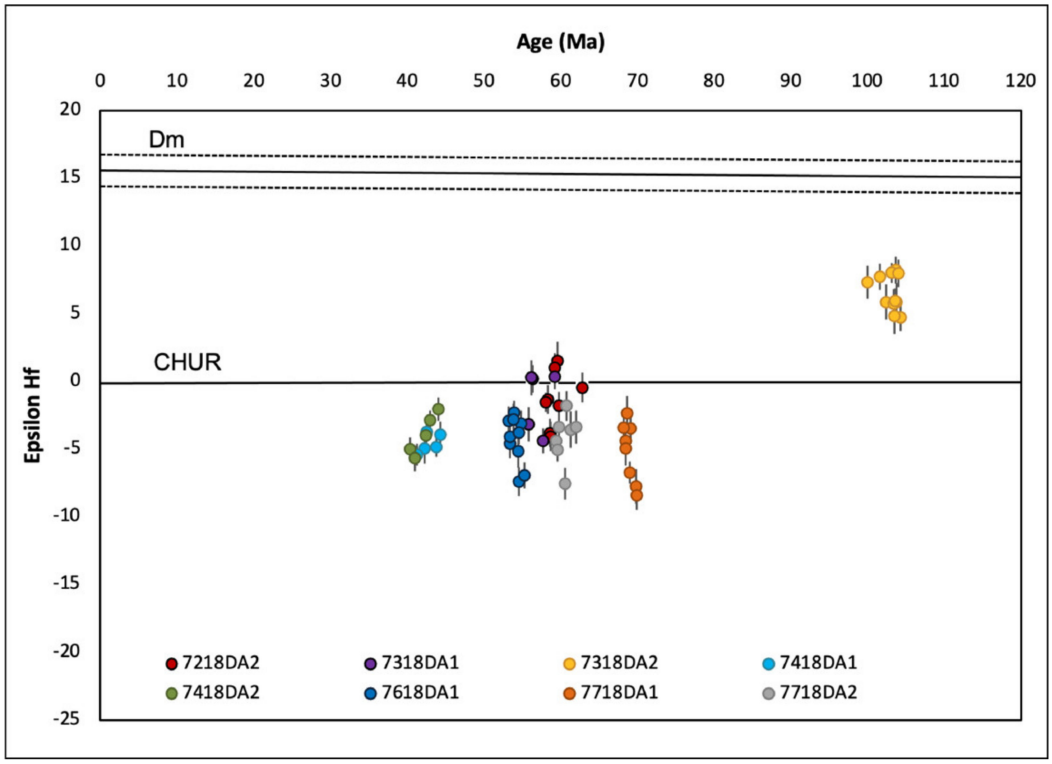

Figure 5. Epsilon Hf ($^{176}Hf/^{177}Hf$) values for igneous zircons plotted against corresponding U-Pb geochronology crystallization ages. More negative values represent more evolved isotopic signatures. Chondritic Uniform Reservoir (CHUR) line depicts expected crustal composition of bulk silicate earth. Depleted Mantle (DM) line represents the natural depletion of incompatible elements within the mantle over time. Note the change in epsilon Hf values from ~100 Ma grains to 70-40 Ma grains. Complete zircon Lu-Hf isotope geochemistry results for individual grains can be found in Supplementary Table S2.

Sample 7218DA2 is porphyritic rhyolite with quartz and feldspar phenocrysts. This sample was collected on top of the ridge-forming horst of the Dajiamang Tso rift, just north of the contact with Kailas Formation strata in the center of mapping area. Zircon U-Pb geochronology for this sample produced a weighted mean age of 59.1 ± 0.4 Ma (n = 22, MSWD = 1.3) (Figure 4). A total of 31 grains were analyzed, 0 were discordant and 22 were selected to calculate a mean sample age. Lu-Hf isotopic analysis for this sample yielded epsilon Hf values from −4.1 ± 1.1 to 1.5 ± 1.4 (Figure 5). No T/REE geochemical data were collected for this sample.

Sample 7718DA2 is aphanitic rhyolite. This sample was collected from the Dajiamang Tso rift footwall, approximately 250 m west of the inferred normal fault that bounds the central horst range to the east (Figure 2). Zircon U-Pb geochronology for this sample produced a weighted mean age of 61.3 ± 0.5 Ma (n = 18, MSWD = 6.7) (Figure 4). A total of 35 grains were analyzed, 6 were discordant and 21 were selected to calculate a mean sample age. Lu-Hf isotopic analysis for this sample yielded epsilon Hf values from −7.5 ± 1.2 to −1.8 ± 1.1 (Figure 5). $La/Yb_{(n)}$ ratios ranged from 5.8 to 10.7, with a mean of 7.9. Crustal thickness estimates (n = 8) determined from this sample range from 37 ± 10.8 km to 47 ± 10.8 km, with a mean calculated thickness of 42 km (Figure 6).

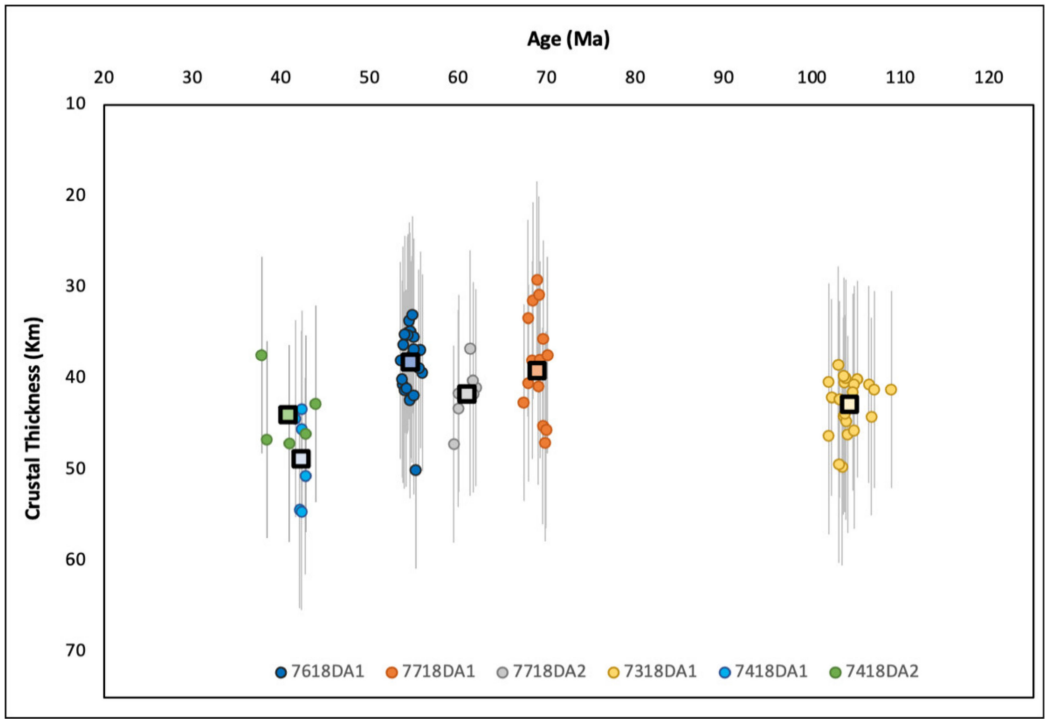

Figure 6. Trace/rare earth element (T/REE) geochemistry crustal thickness estimates for igneous zircons plotted against corresponding U-Pb geochronology crystallization ages. Crustal thickness estimates were calculated using the equations of Sundell et al. (2021) [89] modified from the original equations calibrated by Profeta et al. (2015) [21]. These equations utilize La/Yb ratios as proxies for depth of magma diversification and, thus, crustal thickness at the time of crystallization (see Supplementary Figure S2). Error bars represent ± 10.8 km (2σ) residuals [89]. Larger circles with black outlines represent mean crustal thickness estimates for each sample. Moving right to left through time across the chart, average crustal thickness estimates decrease thickness from ~100 Ma to ~70 Ma, followed by increasing thickness estimates until ~40 Ma. Complete zircon T/REE geochemistry results for individual grains can be found in Supplementary Table S3.

Sample 7718DA1 is fine-grained rhyolite with rare phenocrysts of quartz and biotite. This sample was collected ~2 km north of the lake that occupies the Dajiamang Tso rift valley and is the northernmost sample. Zircon U-Pb geochronology for this sample produced a weighted mean age of 69.4 ± 0.4 Ma (n = 27, MSWD = 6.0) (Figure 4). A total of 34 grains were analyzed, 1 was discordant and 27 were selected to calculate a mean sample age. Lu-Hf isotopic analysis for this sample yielded epsilon Hf values from −8.4 ± 1.1 to −2.4 ± 1.3 (Figure 5). $La/Yb_{(n)}$ ratios ranged from 3.7 to 13.8, with a mean of 7.1. Crustal thickness estimates (n = 15) determined from this sample range from 29 ± 10.8 km to 47 ± 10.8 km, with a mean calculated thickness of 39 km (Figure 6).

4.2.2. Group 2: Gangdese Batholith Granodiorites and Associated Dikes and Fault Rocks

Sample 7418DA1 is a is quartz-feldspar-biotite granite. This sample was collected from the Dajiamang Tso rift footwall in the central–eastern portion of the mapping area. Zircon U-Pb geochronology for this sample produced a weighted mean age of 42.3 ± 0.5 Ma (n = 10, MSWD = 6.5) (Figure 4). A total of 15 grains were analyzed, 0 were discordant, 1 grain was determined to be inherited (107.9 ± 1.1 Ma) (not shown in Figure 4), and 9 were selected to calculate a mean sample age. Lu-Hf isotopic analysis for this sample yielded epsilon Hf values from −5.4 ± 0.8 to −3.7 ± 0.7 (Figure 5). $La/Yb_{(n)}$ ratios ranged from 8.5 to 16.5, with a mean of 12.2. Crustal thickness estimates (n = 6) determined from this sample range from 43 ± 10.8 km to 54 ± 10.8 km, with a mean calculated thickness of 48 km (Figure 6).

Sample 7418DA2 is a medium-gray-green, aphanitic dike that intrudes sample 7418DA1. This sample was collected in the Dajiamang Tso rift footwall. Zircon U-Pb geochronology

for this sample produced a weighted mean age of 43.2 ± 0.7 Ma (n = 6, MSWD = 5.7) (Figure 4). A total of 12 grains were analyzed, 0 were discordant and 6 were selected to calculate a mean sample age. Lu-Hf isotopic analysis for this sample yielded epsilon Hf values from −5.7 ± 0.9 to −2.1 ± 0.9 (Figure 5). $La/Yb_{(n)}$ ratios ranged from 6.0 to 10.6, with a mean of 9.0. Crustal thickness estimates (n = 5) determined from this sample range from 37 ± 10.8 km to 47 ± 10.8 km, with a mean calculated thickness of 44 km (Figure 6).

Sample 7618DA1 is undeformed granodiorite containing quartz, feldspar, biotite, and hornblende. This sample was collected from the Dajiamang Tso rift footwall, approximately 550 m west of the inferred normal fault that bounds the central horst range to the east and approximately 2 km northwest of 7718DA2 (Figure 2). Zircon U-Pb geochronology for this sample produced a weighted mean age of 54.4 ± 0.2 Ma (n = 34, MSWD = 4.2) (Figure 4). A total of 34 grains were analyzed, 0 were discordant and 34 were selected to calculate a mean sample age. Lu-Hf isotopic analysis for this sample yielded epsilon Hf values from −7.4 ± 1.1 to −2.3 ± 0.9 (Figure 5). $La/Yb_{(n)}$ ratios ranged from 4.6 to 12.6, with a mean of 6.5. Crustal thickness estimates (n = 23) determined from this sample range from 33 ± 10.8 km to 50 ± 10.8 km, with a mean calculated thickness of 38 km (Figure 6).

Sample 7418DA3 is silicified breccia with hematite, collected from a 0.75 m fault zone where the central range of the Dajiamang Tso rift changes strike from NW-SE to N-S in the northern section of the mapping area. Zircon U-Pb geochronology for this sample produced a weighted mean age of 57.8 ± 0.4 Ma (n = 14, MSWD = 1.1) (Figure 4). A total of 34 grains were analyzed, 0 were discordant, 3 grains were determined to be inherited (2007.2 ± 13.7, 1101.1 ± 16.0 and 1089.8 ± 17.8 Ma) (not shown in Figure 4), and 14 were selected to calculate a mean sample age. No Lu-Hf or T/REE geochemical data were collected for this sample.

4.2.3. Group 3: Xigaze Group Forearc Rocks

Sample 7318DA2 is white volcanic tuff with quartz, feldspar, and biotite phenocrysts interbedded with medium grained lithic sandstone, interpreted to represent Xigaze Group forearc basin strata [66]. This sample was collected ~100 m south of the Great Counter thrust in the southern portion of the mapping area. Zircon U-Pb geochronology for this sample produced a weighted mean age of 103.7 ± 0.4 Ma (n = 33, MSWD = 2.1) (Figure 4). A total of 35 grains were analyzed, 0 were discordant and 33 were selected to calculate a mean sample age. Lu-Hf isotopic analysis for this sample yielded epsilon Hf values from 4.7 ± 1.0 to 8.2 ± 3.9 (Figure 5). $La/Yb_{(n)}$ ratios ranged from 6.4 to 12.4, with a mean of 8.4. Crustal thickness estimates (n = 22) determined from this sample range from 38 ± 10.8 km to 50 ± 10.8 km, with a mean calculated thickness of 43 km (Figure 6).

4.3. ZHe Thermochronology and HeFTy Thermal Modeling Results

ZHe cooling ages were calculated for seven igneous samples collected from the Dajiamang Tso rift field area. These samples are divided into two groups: (A) samples collected from within the footwall/central horst of the Dajiamang Tso rift (7318DA1, 7218DA2, 7718DA2, 7418DA1, 7618DA1), and (B) samples collected from within the hanging wall of the Dajiamang Tso rift and Great Counter thrust (7718DA1, 7318DA2). ZHe cooling ages were determined for five zircons per sample, with reported mean cooling ages and errors representing the averages of all grains included from each sample.

Samples collected from within the horst block of the Dajiamang Tso rift display a range in ZHe cooling ages from 15.9 ± 0.2 to 8.4 ± 0.1 Ma. Ages from this group show a roughly positive correlation with sample elevation, as well as a positive correlation with the average horizontal distance measured perpendicular to range bounding normal faults (Figure 7). No correlations with grain size or eU are present. Samples collected from the hanging walls of the Dajiamang Tso rift and Great Counter thrust record cooling ages from approximately 30–28 Ma. No major trends are visible in these data given the small sample size (n = 2). The following sections report ZHe cooling ages and HeFTy inverse modeling

results for each sample. Complete analytical results for ZHe thermochronology and HeFTy input parameters can be found in Supplementary Tables S4 and S5, respectively.

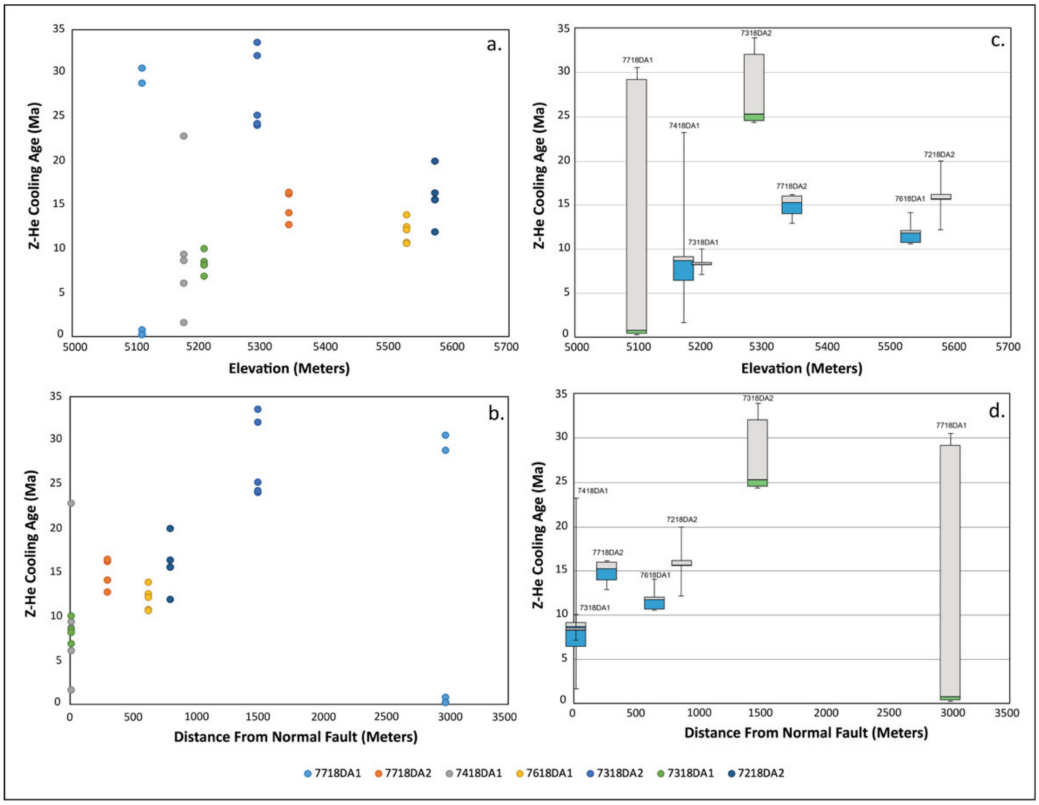

Figure 7. ZHe thermochronology cooling ages plotted (**a**) vs. elevation and (**b**) vs. distance measured orthogonal from the trace of the horst-bounding normal fault. Panels (**c**,**d**) are box and whisker plots visually depicting the same data presented in panels (**a**,**b**). Samples depicted with blue and gray box and whisker plots were collected from the central horst of the Dajiamang Tso rift, while the green and gray box and whisker plots represent the two samples collected from the hanging walls of the Dajiamang Tso rift and Great Counter thrust. The line dividing the two colors within each box and whisker plot represents the median, the lower and upper box boundaries represent the 1st and 3rd quartiles, respectively, and the error bars represent the minimum and maximum values of the analyzed grains. Note the roughly positive correlations within the footwall samples (blue/gray) between ZHe cooling age and (1) elevation and (2) distance from the normal fault.

4.3.1. Group A: Dajiamang Tso Footwall Rocks

Analysis of five zircon grains separated from sample 7318DA1, the porphyritic diorite collected just north of the Kailas basal contact, produced a range in cooling ages from 10.05 ± 0.12 to 6.91 ± 0.08 Ma. All five analyses were used to calculate a mean sample cooling age of 8.4 ± 0.1 Ma. HeFTy modeling results for this sample display significant variation in potential time–temperature paths from zircon's crystallization at ~58 Ma to its passage through the He partial retention zone (HePRZ) at ~8 Ma (Figure 8a). There is, however, significant overlap of "good" and "acceptable" paths beginning at ~36 Ma, suggesting monotonic cooling until the sample reached surface conditions at present. Using this concentration of paths, we estimate an exhumation rate of 0.61 km/Myr for the time span from 36 Ma to present.

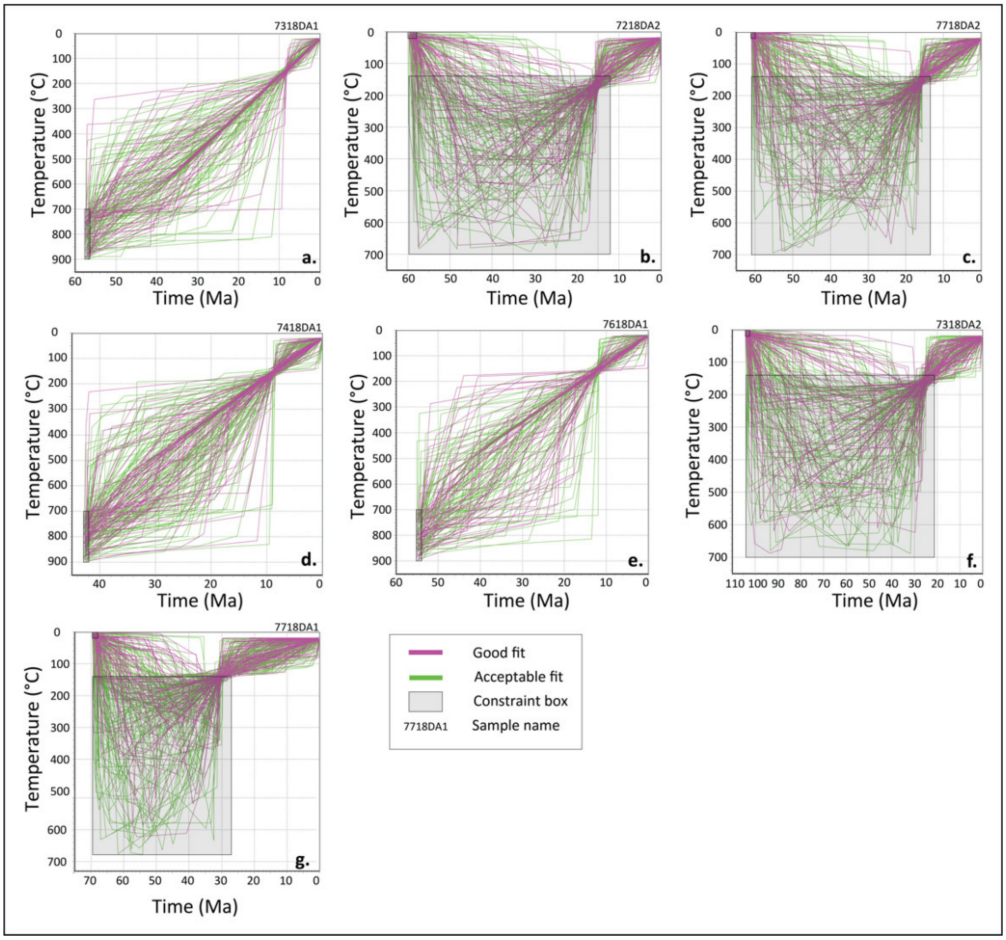

Figure 8. HeFTy [87] inverse modeling results for seven samples (**a**–**g**) displaying "good" (purple) and "acceptable" (green) time–temperature paths for each sample based on n = 10,000 model runs. Black boxes with gray shading represent geologic controls: For intrusive samples, U-Pb geochronology ages were used in conjunction with assumed zircon crystallization temperatures between 900–700 °C to constrain path start points. For extrusive samples, U-Pb geochronology ages were used with the assumption that samples were erupted at surface conditions (0–25 °C) to constrain path start points. Subsequent constraint boxes were implemented for extrusive samples because ZHe cooling ages require burial up to at least 140° (within the ZHe partial retention zone (PRZ)) following crystallization. All model runs require T-t paths to terminate at surface conditions (25 °C) at 0 Ma. "Best fit" and "weighted mean" paths are not displayed to allow the viewer to better identify concentrations of "good-fit" path clusters.

Analysis of five zircon grains separated from sample 7218DA2, the porphyritic rhyolite collected from the top of the Dajiamang Tso horst, produced a range in cooling ages from 19.99 ± 0.25 to 11.95 ± 0.15 Ma. All five analyses were used to calculate a mean sample cooling age of 15.9 ± 0.2 Ma. HeFTy modeling results for this sample display considerable variation in potential time–temperature paths from zircon's crystallization at ~59 Ma, subsequent burial, and ascent through the HePRZ (140–200 °C) at ~16 Ma (Figure 8b). No major concentrations of "good" or "acceptable" paths were observed to calculate exhumation rates for this sample.

An analysis of four zircon grains separated from sample 7718DA2, the aphanitic rhyolite collected north of the mapping area, produced a range in cooling ages from 16.48 ± 0.21 to 12.76 ± 0.16 Ma. For this sample, we report a mean cooling age of 14.9 ± 0.2 Ma. HeFTy modeling results for this sample display considerable variation in potential time–temperature paths following zircon's crystallization at ~60 Ma and subsequent burial prior to exhumation at ~15 Ma (Figure 8c). No major concentrations of "good" or "acceptable" paths were observed to calculate exhumation rates for this sample.

Analysis of five zircon grains separated from sample 7418DA1, the quartz-feldspar-biotite granite collected in the central–eastern portion of the mapping area, produced significant intrasample variation in cooling ages, ranging from 22.86 ± 0.41 to 1.62 ± 0.03 Ma. Effective uranium concentrations display a large range from approximately 800 to 9900 ppm. Including all five analyses, we report a mean cooling age of 9.7 ± 0.2 Ma for this sample. HeFTy modeling results for this sample display significant variation in potential time–temperature paths from zircon's crystallization at ~42 Ma to its passage through the HePRZ at ~9 Ma (Figure 8d). There is, however, significant overlap of "good" and "acceptable" paths beginning at ~26 Ma, suggesting monotonic cooling until the sample reached surface conditions at present. Using this concentration of paths, we estimate an exhumation rate of 0.62 km/Myr for the time span from 26 Ma to present.

The analysis of five zircon grains separated from sample 7618DA1, the undeformed granodiorite collected just north of the mapping area, produced a range in cooling ages from 13.90 ± 0.16 to 10.63 ± 0.12 Ma. For this sample, we report a mean cooling age of 12.0 ± 0.1 Ma. HeFTy modeling results for this sample display a significant variation in potential time–temperature paths from zircon's crystallization at ~54 Ma to its passage through the HePRZ at ~12 Ma (Figure 8e). The sample displays significant overlap of "good" and "acceptable" paths beginning at ~36 Ma, suggesting monotonic cooling until the sample reached surface conditions at present. Using this concentration of paths, we estimate an exhumation rate of 0.44 km/Myr for the time span from 36 Ma to present.

4.3.2. Group A: Local Hanging Wall Rocks

Sample 7318DA2 is the southernmost sample and was collected in the hanging wall proximal to the Great Counter thrust. Analysis of five zircon grains separated from this sample produced a range in cooling ages from 33.56 ± 0.40 to 24.12 ± 0.29 Ma. For this sample, we report a mean cooling age of 27.9 ± 0.3 Ma. HeFTy modeling results for this sample display considerable variation in potential time–temperature paths following zircon's crystallization at ~103 Ma, subsequent burial, and its ascent through the HePRZ at ~28 Ma (Figure 8f). No major concentrations of "good" or "acceptable" paths were observed to calculate exhumation rates for this sample.

Sample 7718DA1 is the northernmost sample and was collected in the low elevation hanging wall of the Dajiamang Tso rift. An analysis of five zircon grains separated from this sample produced a significant intrasample variation in cooling ages, ranging from 30.62 ± 0.36 to 0.19 ± 0.01 Ma. Three of the five grains yielded very little He and near-zero ages compared to other grains and were, therefore, excluded. For this sample, we report a mean cooling age of 29.8 ± 0.4 Ma. HeFTy modeling results for this sample display considerable variation in potential time–temperature paths following zircon's crystallization at ~69 Ma, subsequent burial, and its ascent through the HePRZ at ~30 Ma (Figure 8g). The majority of "good" paths are concentrated cooler than 300 °C, possibly indicating that the sample was buried at relatively shallow depths (≤~12 km).

5. Discussion

5.1. Tectonic Integration

5.1.1. Neo-Tethyan Subduction along the Southern Margin of the Lhasa Terrain

The oldest igneous crystallization age from this study (103.5 ± 0.4 Ma) comes from a re-worked volcanic tuff collected from within Xigaze forearc basin stratigraphy, reflecting coeval volcanism in the Gangdese Range during the mid-Cretaceous period. At this period in the development of the southern Lhasa terrane, ongoing north-directed subduction of Neo-Tethyan oceanic lithosphere produced Gangdese Arc magmatism until ~90 Ma, followed by a period of decreased forearc deposition rates and a lull in Gangdese magmatism that persisted until ~70 Ma [7]. U-Pb geochronology ages of approximately 70–42 Ma from granodiorites of the Gangdese Batholith and overlying volcanic rocks of the Linzizong Formation suggest there was active magmatism along the Gangdese magmatic arc preceding and throughout the proposed period for the initiation of India-Eurasia collision

(~58 Ma) [69,91,92]. A recent geologic synthesis of Tibet by Kapp and DeCelles (2019) [7] provided two leading hypotheses to explain the lull and associated high-T metamorphism and adakitic magmatism in SE Tibet: (1) Neo-Tethyan flat slab subduction and (2) formation and subsequent closure of a backarc basin within the Gangdese arc (the "Xigaze backarc basin"). These hypotheses require dramatically different tectonic configurations and will be further addressed within the context of this study in Section 5.4.

5.1.2. Post-Collisional Deformation along the Gangdese Thrust and Great Counter Thrust

The oldest ZHe cooling age produced from this study (29.8 ± 0.4 Ma) comes from sample 7718DA1, the rhyolite collected ~5 km north of the mapping area in the hanging wall of the Dajiamang Tso rift. This sample displays a significantly older age than nearby footwall samples, suggesting different structural mechanisms for cooling. It is possible that this relatively older cooling age represents south-directed exhumation in the hanging wall of the north-dipping Gangdese Thrust (GT), as previous work on this regional structure suggests that the southernmost splay of the thrust fault became active by ~27 Ma [93]. This relatively older cooling age of ~30 Ma could potentially represent cooling via exhumation along an older, unmapped splay of the GT (Figure 7).

The sample with the second oldest ZHe cooling age was collected from Xigaze forearc strata in the hanging wall of the south-dipping Great Counter thrust [71]. The analysis of this sample produced a mean cooling age of 27.9 ± 0.3 Ma, which we interpret to represent hanging wall erosion during northward thrusting along the Great Counter thrust. This cooling age appears slightly older than previous estimates for thrusting along the Great Counter thrust (23–17 Ma) [71,94,95], but falls within the range of approximately 30–10 Ma for other local ZHe cooling ages from Xigaze forearc basin strata near Saga [70]. Thermal modeling conducted by Orme (2019) [70] suggests that Xigaze forearc samples were buried to maximum temperatures of 140–200 °C by 35–21 Ma, immediately followed by exhumation, indicating that the cooling age produced in this study is compatible with the burial and exhumation of Xigaze forearc strata in this region.

The last group of ZHe cooling ages comes from samples collected within the central horst of the Dajiamang Tso rift. These samples display cooling ages from 15.9 ± 0.2 Ma to 8.4 ± 0.1 Ma, which we attribute to footwall exhumation of the Dajiamang Tso rift. Prior to their late Miocene exhumation via east–west extension, HeFTy thermal modeling suggests that volcanic rock samples were buried up to 5–7 km by overlying volcanic rocks and/or Kailas Formation strata (assuming a 25 °C/km geothermal gradient) (Figures 2 and 7). Diffusion of heat (i.e., contact metamorphism) from igneous intrusions also could have achieved resetting of ZHe cooling ages; however, we observed no spatial trends in ZHe data away from intrusive rock units, causing us to favor the interpretation of reheating via burial. The Kailas basin has been variably interpreted as a peripheral foreland basin [96,97], an extensional basin related to rollback of Greater Indian Lithosphere [60], a foreland basin related to a doubly-vergent orogenic wedge at the time of India-Eurasia collision [98], and most recently as a flexural basin produced by Greater India rollback, with slab breakoff causing flexural rebound and thrusting, ultimately inverting Kailas strata [34]. While the formation history of the Kailas basin remains unclear, U-Pb geochronology of a tuff bed constrains the depositional age of basin strata to 26–24 Ma [60]. We interpret that Kailas sediments combined with overlying Linzizong volcanic rocks provided the overburden necessary to reset the (U-Th)/He system of more deeply buried Linzizong volcanic samples prior to their exhumation in the Dajiamang Tso rift footwall.

5.2. Constraints on the Timing of Extension along North-Striking Rifts

5.2.1. Gangdese Rifts

The geology, geochronology, and thermochronology of the Dajiamang Tso rift are consistent with a normal fault characterized by a central horst bound by NNE- and SSW-dipping normal faults. ZHe thermochrnology results for igneous rocks collected from within the footwall of the Dajiamang Tso rift display a range in cooling ages from ap-

proximately 16–8 Ma, providing a minimum age for the onset of east–west extension in southern Tibet. This minimum age of ~16 Ma appears consistent with the findings of numerous studies of other Gangdese rifts (Figures 1 and 9). Similar (±2 Ma) minimum ages of extension produced by previous studies include a U-Pb crystallization age of ~18 Ma for north-striking dikes located near the Daggyai Tso graben [41], an ^{40}Ar-^{39}Ar age of ~15 Ma for movement along the Lopu Kangri rift [43,44], and an ^{40}Ar-^{39}Ar age of ~14 Ma for north-striking mineralized fractures near the Thakkhola graben (Figures 1 and 9) [33]. Many of these Gangdese rifts also show evidence of recent exhumation and seismogenic activity, including young ZHe cooling ages [45] and fault scarps offsetting quaternary landforms consistent with active east–west extension [74,99].

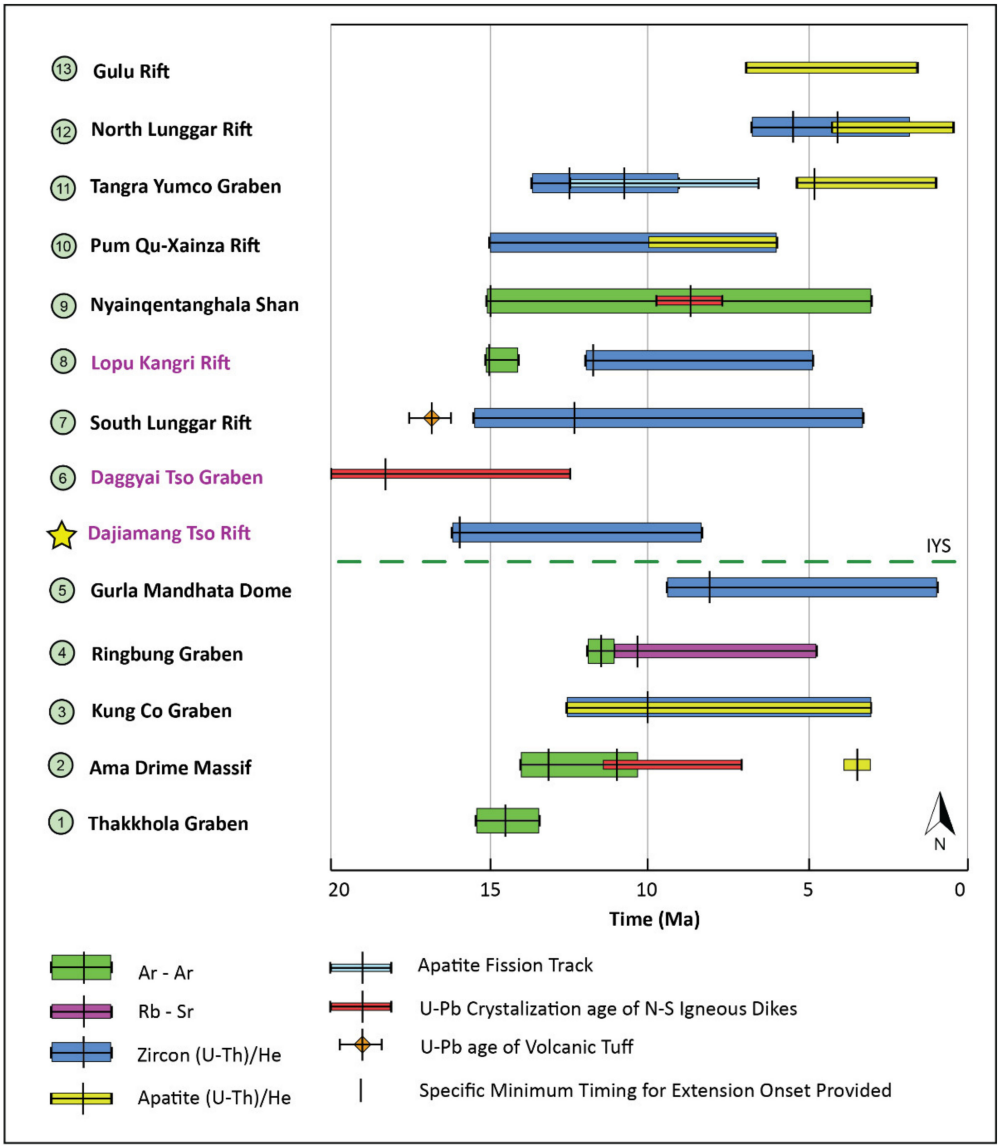

Figure 9. Regional correlation figure comparing ZHe cooling ages from this study to minimum timing estimates for the onset of east–west extension from previously studied rifts throughout central and southern Tibet. Rift numbers increase from SSW–NNE (measured orthogonal to the suture zone) and correspond to studies referenced in Figure 1. Gangdese rift names are labeled in purple (corresponding to Figure 1) and Tibetan rift names are labeled in black. The Indus-Yarlung suture zone is also included for spatial reference. Horizontal colored bars represent the range of measurements (including errors) while vertical black ticks represent the earliest evidence of extension observed for each technique. 1. Thakkhola graben [34], 2. Arma Drime massif [35], 3. Kung Co graben [36], 4. Ringbung graben [37], 5. Gurla Mandhata dome [38,39], 6. Daggyai Tso graben [40,41], 7. South Lunggar rift [24], 8. Lopu Kangri rift [42–44], 9. Nyainquentanghala Shan [45,46], 10. Pum Qu-Xanza rift [47], 11. Tangra Yumco graben [27,48], 12. North Lunggar rift [23,49], 13. Gulu rift [50].

5.2.2. Tibetan Rifts

To better understand possible linkages in extensional processes between the two scales of rifts, we compare results produced from this research to previous thermochronology studies of Tibetan rifts. In southwestern Tibet, ZHe cooling ages coupled with U-Pb geochronology of a tuff in the western basin of the South Lunggar rift suggest that east–west extension was underway by ~17 Ma [24]. In the North Lunggar rift, Kapp et al. (2008) [50] and Sundell et al. (2013) [23] reported minimum extensional ages of ~10 Ma for the same Tibetan rift system, suggesting that considerable N-S variation in minimum timing of extension may exist within these extensional structures (Figure 9). Approximately 300 km east, Tangra Yumco represents another regional-scale normal fault. Wolff et al. (2019) [27] interpreted the extension along this rift system as underway by ~13 Ma based on zircon and apatite-He thermochronology and Apatite Fission Track data. The Pum Qu-Xainza and Nyainqentanghla Shan rifts are located farther to the east and display minimum ages of extension of ~ 15 Ma (Figures 1 and 9) [46,47].

ZHe cooling ages from the Dajiamang Tso rift reported here overlap with published cooling ages for other Gangdese and Tibetan rifts. Based on this study alone, we cannot confidently identify any significant difference in timing for the initiation of extension between the two classes of rifts. When observing both rift classes together, we can, however, identify a spatial relationship throughout the Tethyan Himalaya, with north-striking rifts displaying progressively younger extension estimates moving from SSW to NNE (orthogonal to the Indus-Yarlung suture) (Figure 9). This trend is also present, albeit less well-defined, for rifts in the Lhasa terrane north of the Indus-Yarlung suture zone.

5.3. Crustal Evolution (Lu-Hf) and Crustal Thickness Trends (T/REE)

Lu-Hf isotope geochemistry is a valuable tool for evaluating the evolution of continental crust [100]. Typically, Lu-Hf isotope data are presented as epsilon Hf values vs. corresponding U-Pb age, with more evolved (negative) epsilon Hf values at the time of crystallization representing more incorporation of older and more evolved crustal material. Epsilon Hf values for the oldest sample from this study (~103 Ma) and the youngest samples (~43–42 Ma) are generally in agreement with the compiled dataset for southern Tibet; however, samples with U-Pb ages from 69–56 Ma display more evolved signatures than similarly aged regional data (Figure 10a). As crustal thickness estimates from the Dajiamang Tso rift appear consistent with regional data at this time (Figure 10b), the less evolved signatures from the Tibetan Magmatism Database could be a function of a sample location within a large sampling area throughout southern Tibet. Combined Hf datasets for this region also display a lack of evolved epsilon Hf values from ~100 Ma to ~70 Ma, followed by the appearance of increasingly evolved values towards the present. The lack of evolved epsilon Hf values combined with the presence of numerous samples with depleted epsilon Hf values for this time period may suggest increased tapping of juvenile asthenosphere, or less crust-mantle differentiation, implying assimilation with relatively thin and/or young crust.

Single-grain zircon T/REE crustal thickness estimates from our study also appear in agreement with regional whole rock data downloaded from the Tibetan Magmatism Database, highlighting the applicability of zircon petrochronology (Figure 10b) [90]. From ~190–160 Ma, the crustal thickness appears to increase from ~35 to ~45 km, followed by a lack of substantial data until ~105 Ma. From ~105–70 Ma (a period that roughly corresponds with the lack of evolved epsilon Hf values), crustal thickness appears to decrease, followed by an increase until ~15 Ma when data are no longer available. Modern crustal thickness estimates based on geophysical of observations range from ~65 km [2,3] to ~85 km [4] and appear consistent with continued thickening since the last calculated crustal thickness estimate (55–70 km) at 15 Ma.

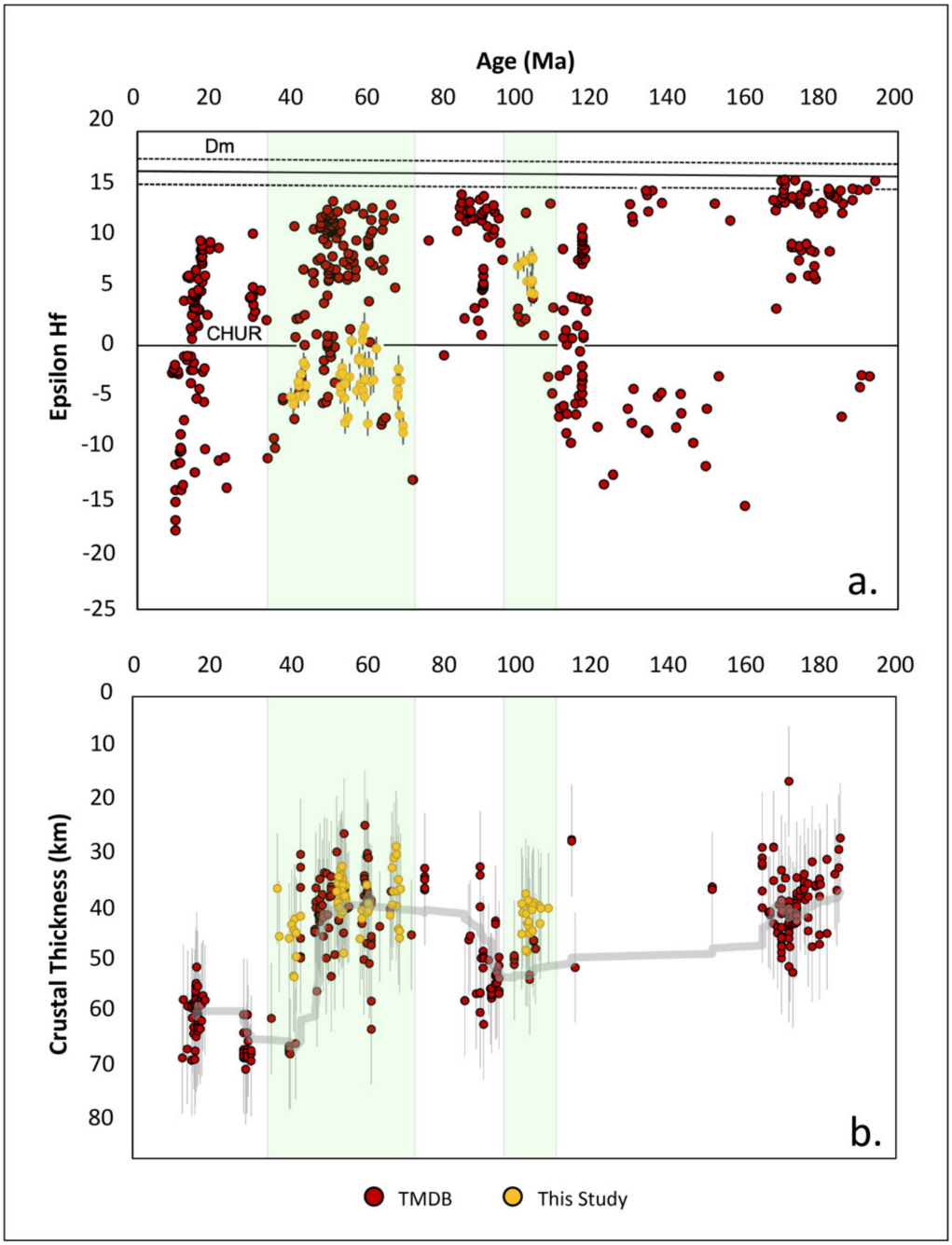

Figure 10. (**a**) Epsilon Hf vs. U-Pb geochronology plots for igneous zircons from this study in the context of regional data downloaded from the Tibetan Magmatism Database (TMDB) (Chapman and Kapp, 2017). CHUR and Dm explanations can be referenced in Figure 5. Lu-Hf filtering criteria for TMDB samples can be referenced in the methods section of this paper; (**b**) T/REE geochemistry crustal thickness estimates vs. U-Pb geochronology crystallization age plots from this study in the context of crustal thickness estimates for regional data downloaded from the Tibetan Magmatism Database (TMDB) (Chapman and Kapp, 2017). TMDB crustal thicknesses were calculated using the equations from Sundell et al. (2021), with data filtered to exclude ultramafic/mantle derived melts, high silica granites, and rocks formed by partial melting of pre-existing meta-sedimentary rocks. Error bars represent ±10.8 km residuals (Sundell et al., 2021). Gray trendline represents a moving average with a sampling period of 30 analyses.

5.4. Tectonic Implications

Geochemical data from this study combined with compiled data from the Tibetan Magmatism Database provide key insights into the controversial period preceding the India-Eurasia collision. The lack of evolved epsilon Hf values from Tibetan Magmatism Database

data paired with decreasing crustal thickness estimates from 100–70 Ma support a tectonic model for the mid-Cretaceous evolution of the southern Lhasa terrane invoking crustal thinning and upper plate extension. These findings question the traditional interpretation of a simple, Andean-style margin along the southern Lhasa terrane [101] and are more consistent with the opening of a back-arc basin inboard of the Xigaze volcanic arc [6,88]. This tectonic configuration suggests that continental India initially collided with the rifted Xigaze arc at ~58 Ma, followed by subduction of back-arc oceanic lithosphere until the Xigaze-India collision with Eurasia and the cessation of Gangdese Arc magmatism at ~38 Ma [44]. Additional geologic mapping is needed to determine the viability of the Xigaze backarc basin model, but our data highlight its relevance as an important hypothesis for future studies.

Results from this study also provide tests of models for the Cenozoic tectonic evolution of the Himalayan-Tibetan orogen. If Miocene extension were due to the gravitational collapse of the plateau [28–30], we would expect peak crustal thickness to coincide with the timing of extension, with subsequent collapse leading to thinner crust at present. Our results show no indication of crustal thinning following the onset of east–west extension, requiring an alternative explanation for either maintenance or addition of crustal thickness since the establishment of Miocene normal faults. Additionally, if the upper plate extension was due to convective removal of the lower layer of Tibet's over-thickened lithosphere [31], we would expect to see a juvenile excursion in Hf isotope data as well as a possible decrease in crustal thickness preceding or coincident with the onset of extension, neither of which are apparent from our compiled datasets.

Data from our study best support a tectonic model in which the addition of crustal material into the Himalayan-Tibetan orogen is facilitated by an underthrusting Indian lithosphere (for a visual, see Styron et al., 2015, Figure 3) [2,25,32]. In this model, crustal thickness in southern Tibet likely reached a critical threshold in the period directly preceding the onset of east–west extension, with modern crustal thicknesses representing an underthrusting Indian lithosphere balanced by upper plate extension. This model would also suggest that the earliest evidence of east–west extension would be localized to high elevation regions in the southern portion of the plateau (i.e., Gangdese Range), with progressive northward underthrusting of Indian lithosphere manifesting on the surface as progressively younger thermochronology ages from south to north. While this trend cannot be clearly observed from ages summarized in this study (Figure 9), future work to constrain the timing of the initiation of east–west extension throughout the plateau may further elucidate the contributing tectonic processes.

6. Conclusions

The Dajiamang Tso rift records development of the southern-central Tibetan Plateau from mid-Cretaceous to Miocene time. U-Pb ages are interpreted to represent Xigaze Group volcanic activity (~103 Ma) as well as Gangdese Batholith and Linzizong Formation magmatism (~70–40 Ma) along the Lhasa terrane's southern convergent margin. ZHe thermochronology data suggest northward thrusting and erosion of the hanging wall of the Great Counter thrust (~28 Ma), as well as east–west extension occurring along the Dajiamang Tso rift from approximately 16–8 Ma. HeFTy thermal modeling suggests burial of volcanic samples, but 7 km prior to exhumation along north-striking normal faults. Lu-Hf isotope geochemistry results display slightly depleted signatures for the Xigaze sample and slightly enriched signatures for Gangdese and Linzizong samples, while compiled data from the Tibetan Magmatism Database show a lack of evolved signatures from approximately 105–70 Ma. Crustal thickness calculations utilizing T/REE geochemistry [89] presented with regional calculations from the Tibetan Magmatism Database suggest ~15 km of crustal thinning from approximately 100–70 Ma (interpreted to represent rifting of the Xigaze magmatic arc), followed by crustal thickening until present. Geochemical data permit crustal thinning and upper plate extension in the Lhasa terrane prior to India-Eurasia collision [6], and support a tectonic model in which the continued addition of

crustal material into the Himalayan-Tibetan orogen is facilitated by an underthrusting Indian lithosphere [2,25,32].

Supplementary Materials: The following are available online at https://www.mdpi.com/article/10.3390/geosciences11050209/s1, Supplementary Table S1: U-Pb Geochronology Data, Supplementary Table S2: Lu-Hf Isotope Geochemistry Data, Supplementary Table S3: T/REE Geochemistry Data, Supplementary Table S4: ZHe Thermochronology Data, Supplementary Table S5: HeFTy Thermal Modeling Parameters, Figure S1: U-Pb Geochronology Concordia Plots, Figure S2: La/Yb Crustal Thickness Plots.

Author Contributions: Conceptualization, A.K.L., W.B.B. and M.H.T.; methodology, A.K.L., W.B.B. and K.E.S.; formal analysis, W.B.B. and A.K.L.; investigation, A.K.L., D.A.O., K.E.S., X.G. and L.D.; writing—original draft preparation, W.B.B.; writing—review and editing, W.B.B., A.K.L., D.A.O., K.E.S. and M.H.T.; visualization, W.B.B.; supervision, A.K.L.; project administration, A.K.L. and W.B.B.; funding acquisition, A.K.L. All authors have read and agreed to the published version of the manuscript.

Funding: This research was funded by the Montana State University and the National Science Foundation EAR-Tectonics Grant 1917685.

Data Availability Statement: Regional magmatic data for Tibet can be found at the Tibetan Magmatism: https://www.jaychapman.org/tibet-magmatism-database.html (accessed on 23 May 2020.)

Acknowledgments: Constructive advising and suggestions: Andrew Laskowski, Devon Orme, and Mary Hubbard. Laboratory and procedural assistance: Kurt Sundell and Mark Pecha.

Conflicts of Interest: The authors declare no conflict of interest.

References

1. Armijo, R.; Tapponnier, P.; Mercier, J.; Han, T.L. Quaternary extension in southern Tibet: Field observations and tectonic implications. *J. Geophys. Res. Solid Earth* **1986**, *91*, 13803–13872. [CrossRef]
2. Zhao, W.; Mechie, J.; Brown, L.; Guo, J.; Haines, S.; Hearn, T.; Nelson, K. Crustal structure of central Tibet as derived from project INDEPTH wide-angle seismic data. *Geophys. J. Int.* **2001**, *145*, 486–498. [CrossRef]
3. Kind, R.; Yuan, X.; Saul, J.; Nelson, D.; Sobolev, S.; Mechie, J.; Achauer, U. Seismic images of crust and upper mantle beneath Tibet: Evidence for Eurasian plate subduction. *Science* **2002**, *298*, 1219–1221. [CrossRef] [PubMed]
4. Xu, Q.; Zhao, J.; Yuan, X.; Liu, H.; Pei, S. Mapping crustal structure beneath southern Tibet: Seismic evidence for continental crustal underthrusting. *Gondwana Res.* **2015**, *27*, 1487–1493. [CrossRef]
5. Allegre, C.O.; Courtillot, V.; Tapponnier, P.; Hirn, A.; Mattauer, M.; Coulon, C.; Marcoux, J. Structure and evolution of the Himalaya–Tibet orogenic belt. *Nature* **1984**, *307*, 17.
6. Yin, A. Mode of Cenozoic east-west extension in Tibet suggesting a common origin of rifts in Asia during the Indo-Asian collision. *J. Geophys. Res. Solid Earth* **2000**, *105*, 21745–21759. [CrossRef]
7. Kapp, P.; DeCelles, P.G. Mesozoic–Cenozoic geological evolution of the Himalayan-Tibetan orogen and working tectonic hypotheses. *Am. J. Sci.* **2019**, *319*, 159–254. [CrossRef]
8. Zuza, A.V.; Gavillot, Y.; Haproff, P.J.; Wu, C. Kinematic evolution of a continental collision: Constraining the Himalayan-Tibetan orogen via bulk strain rates. *Tectonophysics* **2020**, *797*, 228642. [CrossRef]
9. Armijo, R.; Tapponnier, P.; Han, T. Late Cenozoic right-lateral strike-slip faulting in southern Tibet. *J. Geophys. Res. Solid Earth* **1989**, *94*, 2787–2838. [CrossRef]
10. Taylor, M.; Yin, A.; Ryerson, F.J.; Kapp, P.; Ding, L. Conjugate strike-slip faulting along the Bangong-Nujiang suture zone accommodates coeval east-west extension and north-south shortening in the interior of the Tibetan Plateau. *Tectonics* **2003**, *22*. [CrossRef]
11. Yin, A.; Taylor, M.H. Mechanics of V-shaped conjugate strike-slip faults and the corresponding continuum mode of continental deformation. *Bulletin* **2011**, *123*, 1798–1821. [CrossRef]
12. Brown, L.; Zhao, W.; Nelson, K.; Hauck, M.; Alsdorf, D.; Ross, A.; Che, J. Bright spots, structure, and magmatism in southern Tibet from INDEPTH seismic reflection profiling. *Science* **1996**, *274*, 1688–1690. [CrossRef]
13. Alsdorf, D.; Brown, L.; Nelson, K.D.; Makovsky, Y.; Klemperer, S.; Zhao, W. Crustal deformation of the Lhasa terrane, Tibet plateau from Project INDEPTH deep seismic reflection profiles. *Tectonics* **1998**, *17*, 501–519. [CrossRef]
14. Zhao, W.; Brown, L.; Wu, Z.; Klemperer, S.; Shi, D.; Mechie, J.; Makovsky, Y. Seismology across the northeastern edge of the Tibetan Plateau. *Eos Trans. Am. Geophys. Union* **2008**, *89*, 487. [CrossRef]
15. Karplus, M.; Zhao, W.; Klemperer, S.; Wu, Z.; Mechie, J.; Shi, D.; Chen, C. Injection of Tibetan crust beneath the south Qaidam Basin: Evidence from INDEPTH IV wide-angle seismic data. *J. Geophys. Res. Solid Earth* **2011**, *116*. [CrossRef]

16. Mechie, J.; Zhao, W.; Karplus, M.; Wu, Z.; Meissner, R.; Shi, D.; Xue, G. Crustal shear (S) velocity and Poisson's ratio structure along the INDEPTH IV profile in northeast Tibet as derived from wide-angle seismic data. *Geophys. J. Int.* **2012**, *191*, 369–384. [CrossRef]
17. Mechie, J.; Kind, R.A. A model of the crust and mantle structure down to 700 km depth beneath the Lhasa to Golmud transect across the Tibetan plateau as derived from seismological data. *Tectonophysics* **2013**, *606*, 187–197. [CrossRef]
18. Nábělek, J.; Hetényi, G.; Vergne, J.; Sapkota, S.; Kafle, B.; Jiang, M.; Huang, B.-S.; Su, H.; Chen, J.; The Hi-CLIMB Team. Underplating in the Himalaya-Tibet collision zone revealed by the Hi-CLIMB experiment. *Science* **2009**, *325*, 1371–1374.
19. Chapman, J.B.; Ducea, M.N.; DeCelles, P.G.; Profeta, L. Tracking changes in crustal thickness during orogenic evolution with Sr/Y: An example from the North American Cordillera. *Geology* **2015**, *43*, 919–922.
20. Chiaradia, M. Crustal thickness control on Sr/Y signatures of recent arc magmas: An Earth scale perspective. *Sci. Rep.* **2015**, *5*, 8115. [CrossRef]
21. Profeta, L.; Ducea, M.N.; Chapman, J.B.; Paterson, S.R.; Gonzales, S.M.H.; Kirsch, M.; DeCelles, P.G.; Petrescu, L. Quantifying crustal thickness over time in magmatic arcs. *Sci. Rep.* **2015**, *5*, 17786. [CrossRef]
22. Chapman, J.B.; Gehrels, G.E.; Ducea, M.N.; Giesler, N.; Pullen, A. A new method for estimating parent rock trace element concentrations from zircon. *Chem. Geol.* **2016**, *439*, 59–70. [CrossRef]
23. Sundell, K.E.; Taylor, M.H.; Styron, R.H.; Stockli, D.F.; Kapp, P.; Hager, C.; Ding, L.; Liu, D. Evidence for constriction and Pliocene acceleration of east-west extension in the North Lunggar rift region of west central Tibet. *Tectonics* **2013**, *32*, 1454–1479. [CrossRef]
24. Styron, R.H.; Taylor, M.H.; Sundell, K.E.; Stockli, D.F.; Oalmann, J.A.; Möller, A.; McCallister, A.T.; Ding, L.; Liu, D. Miocene initiation and acceleration of extension in the South Lunggar rift, western Tibet: Evolution of an active detachment system from structural mapping and (U-Th)/He thermochronology. *Tectonics* **2013**, *32*, 880–907. [CrossRef]
25. Styron, R.; Taylor, M.; Sundell, K. Accelerated extension of Tibet linked to the northward underthrusting of Indian crust. *Nat. Geosci.* **2015**, *8*, 131. [CrossRef]
26. Laskowski, A.K. *Tectonic Evolution of the Yarlung Suture Zone, Lopu Range and Lazi Regions, Central Southern Tibet*; The University of Arizona: Tucson, AZ, USA, 2016.
27. Wolff, R.; Hetzel, R.; Dunkl, I.; Xu, Q.; Bröcker, M.; Anczkiewicz, A.A. High-Angle Normal Faulting at the Tangra Yumco Graben (Southern Tibet) since ∼ 15 Ma. *J. Geol.* **2019**, *127*, 15–36. [CrossRef]
28. Molnar, P.; Tapponnier, P. Cenozoic tectonics of Asia: Effects of a continental collision. *Science* **1975**, *189*, 419–426. [CrossRef] [PubMed]
29. Molnar, P.; Tapponnier, P. Active tectonics of Tibet. *J. Geophys. Res. Solid Earth* **1978**, *83*, 5361–5375. [CrossRef]
30. Dewey, J. Extensional collapse of orogens. *Tectonics* **1988**, *7*, 1123–1139. [CrossRef]
31. England, P.; Houseman, G. Extension during continental convergence, with application to the Tibetan Plateau. *J. Geophys. Res. Solid Earth* **1989**, *94*, 17561–17579. [CrossRef]
32. Kapp, P.; Guynn, J.H. Indian punch rifts Tibet. *Geology* **2004**, *32*, 993–996. [CrossRef]
33. Murphy, M.; Sanchez, V.; Taylor, M. Syncollisional extension along the India–Asia suture zone, south-central Tibet: Implications for crustal deformation of Tibet. *Earth Planet. Sci. Lett.* **2010**, *290*, 233–243. [CrossRef]
34. Webb, A.A.G.; Guo, H.; Clift, P.D.; Husson, L.; Müller, T.; Costantino, D.; Yin, A.; Xu, Z.; Cao, H.; Wang, Q. The Himalaya in 3D: Slab dynamics controlled mountain building and monsoon intensification. *Lithosphere* **2017**, *9*, 637–651. [CrossRef]
35. Taylor, M.; Yin, A. Active structures of the Himalayan-Tibetan orogen and their relationships to earthquake distribution, contemporary strain field, and Cenozoic volcanism. *Geosphere* **2009**, *5*, 199–214. [CrossRef]
36. Coleman, M.; Hodges, K. Evidence for Tibetan plateau uplift before 14 Myr ago from a new minimum age for east–west extension. *Nature* **1995**, *374*, 49. [CrossRef]
37. Kali, E.; Leloup, P.; Arnaud, N.; Mahéo, G.; Liu, D.; Boutonnet, E.; Li, H. Exhumation history of the deepest central Himalayan rocks, Ama Drime range: Key pressure-temperature-deformation-time constraints on orogenic models. *Tectonics* **2010**, *29*. [CrossRef]
38. Lee, J.; Hager, C.; Wallis, S.R.; Stockli, D.F.; Whitehouse, M.J.; Aoya, M.; Wang, Y. Middle to late Miocene extremely rapid exhumation and thermal reequilibration in the Kung Co rift, southern Tibet. *Tectonics* **2011**, *30*. [CrossRef]
39. Ratschbacher, L.; Krumrei, I.; Blumenwitz, M.; Staiger, M.; Gloaguen, R.; Miller, B.V.; Samson, S.D.; Edwards, M.A.; Appel, E. Rifting and strike-slip shear in central Tibet and the geometry, age and kinematics of upper crustal extension in Tibet. *Geol. Soc. Lond. Spec. Publ.* **2011**, *353*, 127–163. [CrossRef]
40. Murphy, M.; Yin, A.; Kapp, P.; Harrison, T.; Manning, C.; Ryerson, F.J.; Lin, D.; Jinghui, G. Structural evolution of the Gurla Mandhata detachment system, southwest Tibet: Implications for the eastward extent of the Karakoram fault system. *Geol. Soc. Am. Bull.* **2002**, *114*, 428–447. [CrossRef]
41. McCallister, A.T.; Taylor, M.H.; Murphy, M.A.; Styron, R.H.; Stockli, D.F. Thermochronologic constraints on the late Cenozoic exhumation history of the Gurla Mandhata metamorphic core complex, Southwestern Tibet. *Tectonics* **2014**, *33*, 27–52. [CrossRef]
42. Williams, H.; Turner, S.; Kelley, S.; Harris, N. Age and composition of dikes in Southern Tibet: New constraints on the timing of east-west extension and its relationship to postcollisional volcanism. *Geology* **2001**, *29*, 339–342. [CrossRef]
43. Yin, A.; Harrison, T.M. Geologic evolution of the Himalayan-Tibetan orogen. *Annu. Rev. Earth Planet. Sci.* **2000**, *28*, 211–280. [CrossRef]

44. Sanchez, V.; Murphy, M.; Robinson, A.; Lapen, T.; Heizler, M. Tectonic evolution of the India–Asia suture zone since Middle Eocene time, Lopukangri area, south-central Tibet. *J. Asian Earth Sci.* **2013**, *62*, 205–220. [CrossRef]
45. Laskowski, A.K.; Kapp, P.; Ding, L.; Campbell, C.; Liu, X. Tectonic evolution of the Yarlung suture zone, Lopu Range region, southern Tibet. *Tectonics* **2017**, *36*, 108–136. [CrossRef]
46. Harrison, T.M.; Copeland, P.; Kidd, W.; Lovera, O.M. Activation of the Nyainqentanghla shear zone: Implications for uplift of the southern Tibetan Plateau. *Tectonics* **1995**, *14*, 658–676. [CrossRef]
47. Kapp, J.L.D.A.; Harrison, T.M.; Kapp, P.; Grove, M.; Lovera, O.M.; Lin, D. Nyainqentanglha Shan: A window into the tectonic, thermal, and geochemical evolution of the Lhasa block, southern Tibet. *J. Geophys. Res. Solid Earth* **2005**, 110. [CrossRef]
48. Hager, C.; Stockli, D.; Dewane, T.; Gehrels, G.; Ding, L. Anatomy and Crustal Evolution of the Central Lhasa Terrane (S-Tibet) Revealed by Investigations in the Xainza Rift. In Proceedings of the EGU General Assembly Conference, Vienna, Austria, 7–12 April 2019.
49. Dewane, T.; Stockli, D.; Hager, C.; Taylor, M.; Ding, L.; Lee, J.; Wallis, S. Timing of Cenozoic EW Extension in the Tangra Yum Co-Kung Co Rift, south-central Tibet. In Proceedings of the Agu Fall Meeting, San Francisco, CA, USA, 11–15 December 2006.
50. Kapp, P.; Taylor, M.; Stockli, D.; Ding, L. Development of active low-angle normal fault systems during orogenic collapse: Insight from Tibet. *Geology* **2008**, *36*, 7–10. [CrossRef]
51. Stockli, D.F.; Taylor, M.; Yin, A.; Harrison, T.M.; D'Andrea, J.; Kapp, P.; Ding, L. Late Miocene-Pliocene inception of EW extension in Tibet as evidenced by apatite (U-Th)/He data. In Proceedings of the Geological Society of America, Denver, CO, USA, 27–30 October 2002.
52. Lee, H.-Y.; Chung, S.-L.; Lo, C.-H.; Ji, J.; Lee, T.-Y.; Qian, Q.; Zhang, Q. Eocene Neotethyan slab breakoff in southern Tibet inferred from the Linzizong volcanic record. *Tectonophysics* **2009**, *477*, 20–35. [CrossRef]
53. Maluski, H.; Proust, F.; Xiao, X. 39 Ar/40 Ar dating of the trans-Himalayan calc-alkaline magmatism of southern Tibet. *Nature* **1982**, *298*, 152–154. [CrossRef]
54. Coulon, C.; Maluski, H.; Bollinger, C.; Wang, S. Mesozoic and Cenozoic volcanic rocks from central and southern Tibet: 39Ar-40Ar dating, petrological characteristics and geodynamical significance. *Earth Planet. Sci. Lett.* **1986**, *79*, 281–302. [CrossRef]
55. Pan, G.; Ding, J.; Yao, D.; Wang, L. *Guidebook of 1: 1,500,000 Geologic Map of the Qinghai–Xizang (Tibet) Plateau and Adjacent Areas*; Chengdu Cartographic Publishing House: Chengdu, China, 2004.
56. Lee, H.; Chung, S.; Wang, Y.; Zhu, D.; Yang, J.; Song, B.; Liu, D.; Wu, F. Age, petrogenesis and geological significance of the Linzizong volcanic successions in the Linzhou basin, southern Tibet: Evidence from zircon U-Pb dates and Hf isotopes. *Acta Petrol. Sin.* **2007**, *23*, 493–500.
57. Schärer, U.; Xu, R.-H.; Allègre, C.J. UPb geochronology of Gangdese (Transhimalaya) plutonism in the Lhasa-Xigaze region, Tibet. *Earth Planet. Sci. Lett.* **1984**, *69*, 311–320. [CrossRef]
58. Gansser, A. *Geology of the Himalayas*; Wiley InterScience: Hoboken, NJ, USA, 1964.
59. Aitchison, J.C.; Davis, A.M.; Luo, H. New constraints on the India–Asia collision: The lower Miocene Gangrinboche conglomerates, Yarlung Tsangpo suture zone, SE Tibet. *J. Asian Earth Sci.* **2002**, *21*, 251–263. [CrossRef]
60. DeCelles, P.G.; Kapp, P.; Quade, J.; Gehrels, G.E. Oligocene–Miocene Kailas basin, southwestern Tibet: Record of postcollisional upper-plate extension in the Indus-Yarlung suture zone. *GSA Bull.* **2011**, *123*, 1337–1362. [CrossRef]
61. Leary, R.; Orme, D.A.; Laskowski, A.K.; DeCelles, P.G.; Kapp, P.; Carrapa, B.; Dettinger, M. Along-strike diachroneity in deposition of the Kailas Formation in central southern Tibet: Implications for Indian slab dynamics. *Geosphere* **2016**, *12*, 1198–1223. [CrossRef]
62. Shen, T.; Wang, G.; Bernet, M.; Replumaz, A.; Ai, K.; Song, B.; Zhang, K.; Zhang, P. Long-term exhumation history of the Gangdese magmatic arc: Implications for the evolution of the Kailas Basin, western Tibet. *Geol. J.* **2019**, *55*, 7239–7250. [CrossRef]
63. Einsele, G.; Liu, B.; Dürr, S.; Frisch, W.; Liu, G.; Luterbacher, H.; Ratschbacher, L.; Ricken, W.; Wendt, J.; Yu, G.; et al. The Xigaze forearc basin: Evolution and facies architecture (Cretaceous, Tibet). *Sediment. Geol.* **1994**, *90*, 1–32. [CrossRef]
64. Dürr, S.R.B. Provenance of Xigaze fore-arc basin clastic rocks (Cretaceous, south Tibet). *Geol. Soc. Am. Bull.* **1996**, *108*, 669–684. [CrossRef]
65. An, W.; Hu, X.; Garzanti, E.; BouDagher-Fadel, M.K.; Wang, J.; Sun, G. Xigaze forearc basin revisited (South Tibet): Provenance changes and origin of the Xigaze Ophiolite. *Bulletin* **2014**, *126*, 1595–1613. [CrossRef]
66. Orme, D.A.; Laskowski, A.K. Basin analysis of the Albian–Santonian Xigaze forearc, Lazi region, south-central Tibet. *J. Sediment. Res.* **2016**, *86*, 894–913. [CrossRef]
67. Wang, E.; Kamp, P.J.; Xu, G.; Hodges, K.V.; Meng, K.; Chen, L.; Wang, G.; Luo, H. Flexural bending of southern Tibet in a retro foreland setting. *Sci. Rep.* **2015**, *5*, 12076. [CrossRef]
68. Wang, J.-G.; Hu, X.; Garzanti, E.; An, W.; Liu, X.-C. The birth of the Xigaze forearc basin in southern Tibet. *Earth Planet. Sci. Lett.* **2017**, *465*, 38–47. [CrossRef]
69. Orme, D.A.; Carrapa, B.; Kapp, P. Sedimentology, provenance and geochronology of the upper Cretaceous–lower Eocene western Xigaze forearc basin, southern Tibet. *Basin Res.* **2015**, *27*, 387–411. [CrossRef]
70. Orme, D.A. Burial and exhumation history of the Xigaze forearc basin, Yarlung suture zone, Tibet. *Geosci. Front.* **2019**, *10*, 895–908. [CrossRef]
71. Heim, A.; Gansser, A. *Central Himalaya: Geological Observations of the Swiss Expedition 1975, 1936*; Hindustan Publishing Corporation: Delhi, India, 1939.

72. Yin, A.; Harrison, T.M.; Murphy, M.; Grove, M.; Nie, S.; Ryerson, F.; Feng, W.X.; Zeng Le, C. Tertiary deformation history of southeastern and southwestern Tibet during the Indo-Asian collision. *Geol. Soc. Am. Bull.* **1999**, *111*, 1644–1664. [CrossRef]
73. Murphy, M.; Yin, A. Structural evolution and sequence of thrusting in the Tethyan fold-thrust belt and Indus-Yalu suture zone, southwest Tibet. *Geol. Soc. Am. Bull.* **2003**, *115*, 21–34. [CrossRef]
74. Zhang, P.-Z.; Shen, Z.; Wang, M.; Gan, W.; Bürgmann, R.; Molnar, P.; Wang, Q.; Niu, Z.; Sun, J.; Hanrong, S.; et al. Continuous deformation of the Tibetan Plateau from global positioning system data. *Geology* **2004**, *32*, 809–812. [CrossRef]
75. Paces, J.B.; Miller, J.D., Jr. Precise U-Pb ages of Duluth complex and related mafic intrusions, northeastern Minnesota: Geochronological insights to physical, petrogenetic, paleomagnetic, and tectonomagmatic processes associated with the 1.1 Ga midcontinent rift system. *J. Geophys. Res. Solid Earth* **1993**, *98*, 13997–14013. [CrossRef]
76. Schmitz, M.D.; Bowring, S.A.; Ireland, T.R. Evaluation of Duluth Complex anorthositic series (AS3) zircon as a U-Pb geochronological standard: New high-precision isotope dilution thermal ionization mass spectrometry results. *Geochim. Cosmochim. Acta* **2003**, *67*, 3665–3672.
77. Black, L.P.; Kamo, S.L.; Allen, C.M.; Davis, D.W.; Aleinikoff, J.N.; Valley, J.W.; Mundil, R.; Campbell, I.H.; Korscch, R.J.; Williams, I.S. Improved 206Pb/238U microprobe geochronology by the monitoring of a trace-element-related matrix effect; SHRIMP, ID–TIMS, ELA–ICP–MS and oxygen isotope documentation for a series of zircon standards. *Chem. Geol.* **2004**, *205*, 115–140.
78. Gehrels, G.E.; Valencia, V.A.; Ruiz, J. Enhanced precision, accuracy, efficiency, and spatial resolution of U-Pb ages by laser ablation–multicollector–inductively coupled plasma–mass spectrometry. *Geochem. Geophys. Geosyst.* **2008**, *9*. [CrossRef]
79. Gehrels, G.; Valencia, V.; Pullen, A. Detrital zircon geochronology by laser-ablation multicollector ICPMS at the Arizona LaserChron Center. *Paleontol. Soc. Pap.* **2006**, *12*, 67–76. [CrossRef]
80. Gehrels, G.; Pecha, M. Detrital zircon U-Pb geochronology and Hf isotope geochemistry of Paleozoic and Triassic passive margin strata of western North America. *Geosphere* **2014**, *10*, 49–65. [CrossRef]
81. Pullen, A.; Ibáñez-Mejia, M.; Gehrels, G.E.; Giesler, D.; Pecha, M. Optimization of a laser ablation-single collector-inductively coupled plasma-mass spectrometer (Thermo Element 2) for accurate, precise, and efficient zircon U-Th-Pb geochronology. *Geochem. Geophys. Geosyst.* **2018**, *19*, 3689–3705. [CrossRef]
82. Ludwig, K.; Mundil, R. Extracting reliable U-Pb ages and errors from complex populations of zircons from Phanerozoic tuffs. *Geochim. Cosmochim. Acta* **2002**, *66*, A463.
83. Ludwig, K.R. Isoplot 3.00: A geochronological toolkit for Microsoft Excel. *Berkeley Geochronol. Cent. Spec. Publ.* **2003**, *4*, 70.
84. Reiners, P.W. Zircon (U-Th)/He thermochronometry. *Rev. Miner. Geochem.* **2005**, *58*, 151–179. [CrossRef]
85. Hourigan, J.K.; Reiners, P.W.; Brandon, M.T. U-Th zonation-dependent alpha-ejection in (U-Th)/He chronometry. *Geochim Cosmochim. Acta* **2005**, *69*, 3349–3365. [CrossRef]
86. Guenthner, W.R.; Reiners, P.W.; Ketcham, R.A.; Nasdala, L.; Giester, G. Helium diffusion in natural zircon: Radiation damage, anisotropy, and the interpretation of zircon (U-Th)/He thermochronology. *Am. J. Sci.* **2013**, *313*, 145–198. [CrossRef]
87. Ketcham, R.A. Forward and inverse modeling of low-temperature thermochronometry data. *Rev. Miner. Geochem.* **2005**, *58*, 275–314. [CrossRef]
88. Ketcham, R.A.; Gautheron, C.; Tassan-Got, L. Accounting for long alpha-particle stopping distances in (U–Th–Sm)/He geochronology: Refinement of the baseline case. *Geochim. Cosmochim. Acta* **2011**, *75*, 7779–7791. [CrossRef]
89. Sundell, K.; Laskowski, A.K.; Kapp, P.A.; Ducea, M.N. Jurassic to Neogene quantitative crustal thickness estimates in southern Tibet from recalibrated Sr/Y and La/Yb trace element geochemical proxies. *GSA Today* **2020**. [CrossRef]
90. Chapman, J.B.; Kapp, P. Tibetan magmatism database. *Geochem. Geophys. Geosyst.* **2017**, *18*, 4229–4234. [CrossRef]
91. DeCelles, P.G.; Kapp, P.; Gehrels, G.E.; Ding, L. Paleocene-Eocene foreland basin evolution in the Himalaya of southern Tibet and Nepal: Implications for the age of initial India-Asia collision. *Tectonics* **2014**, *33*, 824–849. [CrossRef]
92. Hu, X.; Wang, J.; BouDagher-Fadel, M.; Garzanti, E.; An, W. New insights into the timing of the India–Asia collision from the Paleogene Quxia and Jialazi formations of the Xigaze forearc basin, South Tibet. *Gondwana Res.* **2016**, *32*, 76–92. [CrossRef]
93. Yin, A.; Harrison, T.M.; Ryerson, F.; Wenji, C.; Kidd, W.; Copeland, P. Tertiary structural evolution of the Gangdese thrust system, southeastern Tibet. *J. Geophys. Ress Solid Earth* **1994**, *99*, 18175–18201. [CrossRef]
94. Zhang, R.; Murphy, M.A.; Lapen, T.J.; Sanchez, V.; Heizler, M. Late Eocene crustal thickening followed by Early-Late Oligocene extension along the India-Asia suture zone: Evidence for cyclicity in the Himalayan orogen. *Geosphere* **2011**, *7*, 1249–1268. [CrossRef]
95. Laskowski, A.K.; Kapp, P.; Cai, F. Gangdese culmination model: Oligocene–Miocene duplexing along the India-Asia suture zone, Lazi region, southern Tibet. *GSA Bull.* **2018**, *130*, 1355–1376. [CrossRef]
96. Searle, M.; Windley, B.; Coward, M.; Cooper, D.; Rex, A.; Rex, D.; Tingdong, L.; Xuchang, X.; Jan, M.Q.; Thakur, V.; et al. The closing of Tethys and the tectonics of the Himalaya. *Geol. Soc. Am. Bull.* **1987**, *98*, 678–701. [CrossRef]
97. Harrison, T.M.; Copeland, P.; Kidd, W.; Yin, A. Raising tibet. *Science* **1992**, *255*, 1663–1670. [CrossRef]
98. Wang, C.; Li, X.; Liu, Z.; Li, Y.; Jansa, L.; Dai, J.; Wei, Y. Revision of the Cretaceous–Paleogene stratigraphic framework, facies architecture and provenance of the Xigaze forearc basin along the Yarlung Zangbo suture zone. *Gondwana Res.* **2012**, *22*, 415–433. [CrossRef]
99. Gan, W.; Zhang, P.; Shen, Z.K.; Niu, Z.; Wang, M.; Wan, Y.; Zhou, D.; Cheng, J. Present-day crustal motion within the Tibetan Plateau inferred from GPS measurements. *J. Res. Solid Earth* **2007**, *112*. [CrossRef]

100. Hawkesworth, C.; Kemp, A. Using hafnium and oxygen isotopes in zircons to unravel the record of crustal evolution. *Chem. Geol.* **2006**, *226*, 144–162. [CrossRef]
101. Kapp, P.; DeCelles, P.G.; Leier, A.; Fabijanic, J.; He, S.; Pullen, A.; Gehrels, G.E.; Ding, L. The Gangdese retroarc thrust belt revealed. *GSA Today* **2007**, *17*, 4. [CrossRef]